The Subaru/*XMM-Newton* Deep Field - II. The 37 brightest radio sources

Eleni Vardoulaki[1], Steve Rawlings[1], Chris Simpson[2], David G. Bonfield[1], R. J. Ivison[3,4], Eduardo Ibar[4]

[1] *Astrophysics, Department of Physics, Denys Wilkinson Building, Keble Road, Oxford, OX1 3RH, UK*
[2] *Astrophysics Research Institute, Liverpool John Moores University, Twelve Quays House, Egerton Wharf, Birkenhead CH41 1LD, UK*
[3] *UK Astronomy Technology Centre, Royal Observatory, Blackford Hill, Edinburgh EH9 3HJ*
[4] *Institute for Astronomy, University of Edinburgh, Blackford Hill, Edinburgh EH9 3HJ*

ABSTRACT
We study the 37 brightest radio sources in the Subaru/*XMM-Newton* Deep Field (SXDF). We have spectroscopic redshifts for 24 of 37 objects and photometric redshifts for the remainder, yielding a median redshift z_{med} for the whole sample of $z_{med} \simeq 1.1$ and a median radio luminosity close to the 'FRI/FRII' luminosity divide. Using mid-IR (Spitzer MIPS 24 μm) data we expect to trace nuclear accretion activity, even if it is obscured at optical wavelengths, unless the obscuring column is extreme. Our results suggest that above the FRI/FRII radio luminosity break most of the radio sources are associated with objects that have excess mid-IR emission, only some of which are broad-line objects, although there is one clear low-accretion-rate object with an FRI radio structure. For extended steep-spectrum radio sources, the fraction of objects with mid-IR excess drops dramatically below the FRI/FRII luminosity break, although there exists at least one high-accretion-rate 'radio-quiet' QSO. We have therefore shown that the strong link between radio luminosity (or radio structure) and accretion properties, well known at $z \sim 0.1$, persists to $z \sim 1$. Investigation of mid-IR and blue excesses shows that they are correlated as predicted by a model in which, when significant accretion exists, a torus of dust absorbs $\sim$30% of the light, and the dust above and below the torus scatters $\gtrsim$1% of the light.

Key words:

1 INTRODUCTION

There is growing evidence that all massive galaxies contain a supermassive black hole (SMBH) at their centres (Ferrarese & Merritt 2000; Gebhardt et al. 2000; Magorrian 2006), which implies that these galaxies have all undergone at least one episode of AGN activity. It is believed that this AGN activity is the observational manifestation of feedback processes regulating galaxy and cluster evolution (Best et al. 2005). At low redshifts radio jets emerge from the vicinities of these black holes, where there are indications for a 'duty cycle' for active jet activity that varies from $\sim 0.1 \rightarrow 0.3$ over the 1.4-GHz luminosity range $L_{1.4GHz} \sim 8 \times 10^{23} \rightarrow 8 \times 10^{21} \mathrm{WHz^{-1}sr^{-1}}$ – a critical range as it provides a significant fraction ($\sim$25%) of the luminosity density of the population.

Powerful ($L_{1.4GHz} > 8 \times 10^{23} \mathrm{WHz^{-1}sr^{-1}}$) radio sources are more common at high ($z \gtrsim 1$) redshifts. They are believed to have central SMBHs with uniformly high accretion rates at the highest radio luminosities and relatively low duty cycles (e.g. Rawl-

ings & Saunders 1991). Low-luminosity radio jets can, however, be associated with high-accretion-rate systems, and these so-called 'radio-quiet' quasars appear to have similar FRI-like radio structures to the low-accretion-rate counterparts of similar radio luminosity objects (e.g. Heywood et al. 2007). At low redshift, the most massive ($\gtrsim 10^8 \mathrm{M}_\odot$) SMBHs typically have very low accretion rates with systematically higher average values at $z \gtrsim 2$, the so-called 'quasar epoch' (Yu & Tremaine 2002). These observational results fit in with theoretical ideas that a 'quasar mode' of feedback is prevalent in the distant universe, and that a 'radio mode' of feedback is dominant at low redshift (e.g. Croton et al. 2006).

In the unified model for AGNs (e.g. Antonucci 1993), the central region is surrounded by a dusty torus which absorbs light and re-emits it in the infrared. Above and below the plane of the torus, dust scatters light yielding a blue excess (di Serego Alighieri et al. 1993; Tadhunter et al. 1992; Cimatti et al. 1993; Jannuzi et al. 1995). Such mechanisms make it difficult to observe objects viewed through the torus directly in the optical, UV and soft X-rays. The torus creates anisotropic obscuration of the central regions resulting in two different types of observed objects, type 1 that are viewed face-on and type 2 that are viewed edge-on. Here we use mid-IR observations to search for evidence of accretion in a manner which is far less dependent on orientation. Note, however, that there are claims that hot-dust emission is mildly anisotropic due to the effects of high optical depths and a toroidal geometry (Granato & Danese 1994).

Through the years, there have been many attempts to classify radio sources according to their observed properties: e.g. their structure, energy output and environment. Fanaroff & Riley (1974) classified radio sources according to their structure by measuring the ratio of distance between the regions of highest surface brightness on opposite sides of the central galaxy or quasar to the total extent of the source up to the lowest brightness contour R_{FR}. This way, for FRI radio sources we get $R_{\mathrm{FR}} < 0.5$ which makes them edge-darkened, while FRIIs have $R_{\mathrm{FR}} > 0.5$ meaning they are edge-brightened. Furthermore, they found a strong correlation of structure with radio luminosity: above $\log_{10}(L_{178\mathrm{MHz}}/\mathrm{WHz}^{-1}\mathrm{sr}^{-1}) \approx 25$ ($H_0 = 50$ km s^{-1}Mpc^{-1}, $\Omega_{\mathrm{M}} = 1$ and $\Omega_\Lambda = 0)^\star$ lie the FRIIs, and below that the FRIs.

Ledlow & Owen (1996) found that both FRIs and FRIIs live in similar environments, but the properties of their host galaxies may influence the structural appearance of the radio sources, at least for those near the division of the two FR classes. A more refined

division of radio sources by structure is the one appearing in Owen & Laing (1989). In this case we have Classical Double (CD), Twin Jet (TJ) and Fat Double (FD) radio sources: CDs correspond to FRIIs, TJs to FRIs and FDs to FRI/FRII division objects. Study of the 3CRR, 6CE, 7CRS and TOOT radio samples at $z \sim 0.5$ (McLure et al. 2004) is consistent with the low-redshift result of Owen & Laing (1989) that FRI (FD & TJ) sources reside in hosts which are on average $\simeq 0.5$ mag brighter than those of classical double/FRII sources of comparable radio luminosity.

Other classification schemes, such as the 'dual-population' model (e.g. Jackson & Wall 2001), divide objects according to nuclear accretion rate following the pioneering study of Hine & Longair (1979). The less radio-luminous population is composed of FRIs and FRIIs with weak or absent narrow emission lines, and the more radio-luminous population of strong narrow-emission-line FRII radio galaxies and broad-line quasars, where the division is at $\log_{10}(L_{178\mathrm{MHz}}/\mathrm{WHz}^{-1}\mathrm{sr}^{-1}) \approx 26$ ($H_0 = 70$ km s^{-1}Mpc^{-1}, $\Omega_{\mathrm{M}} = 0.3$ and $\Omega_\Lambda = 0.7$) and corresponds to the Radio Luminosity Function (RLF) break (e.g. Dunlop & Peacock 1990). Best et al. (2003) investigated the dual-population scheme for radio sources using the CENSORS sample, selected from the 1.4 GHz NVSS survey (Condon et al. 1998).

Ogle et al. (2006) studied a sample of FRII narrow-line radio galaxies from the 3CRR survey at redshifts $z < 1$, in order to investigate whether they host hidden quasar nuclei. They found that in most of these radio galaxies, absorption in the mid-IR is present due to dust from a molecular torus. Almost half of their sample of narrow-line FR II radio galaxies is weak at 15 or 30 μm, contrary to single-population unification schemes. They conclude that mid-IR weak radio galaxies may constitute a separate population of jet-dominated sources with low accretion power. In Vardoulaki et al. (2006) we expressed the need to study radio sources in the mid-IR in order to investigate the existence of any hidden accretion activity in low-luminosity radio sources. Spitzer observations at 24 μm are ideal for this task, since they trace warm dust emission which can be obscured only by extreme columns (Ogle et al. 2006).

To address this important issue, we have looked at a complete sample of radio sources in the Subaru/*XMM-Newton* Deep Field (SXDF). The sample studied here is the 37 brightest radio sources from the VLA survey (SXDS) of the SXDF (Simpson et al. 2006) with flux densities greater than 2 mJy at 1.4 GHz. In Section 2 we present new data taken on the SXDS radio sources, namely optical and near-infrared imaging and spectroscopy. We also present a cross-correlation with the radio sample of Tasse et al. (2006), who observed this sky region at 325 MHz, as well as GMRT observations at 610 MHz (Sec. 2.1). Section 3 presents the analysis of our sample including K-band/radio overlays (Sec. 3.1), photometric red-

---

$\star$ This corresponds to $\log_{10}(L_{178\mathrm{MHz}}/\mathrm{WHz}^{-1}\mathrm{sr}^{-1}) \approx 25$ in our adopted cosmology ($H_0 = 70$ km s^{-1}Mpc^{-1}, $\Omega_{\mathrm{M}} = 0.3$ and $\Omega_\Lambda = 0.3$) at the typical redshift ($z \simeq 0.1$) of the FRI/FRII division from the Fanaroff & Riley (1974) study.

shift estimation (Sec. 3.2), and the classification of the SXDS-based sample according to optical and infrared data (Sec. 3.3). In Section 4 we discuss accretion indicators, based on our optical/infrared radio-source classification. In Section 5 we present the conclusions of our study. Finally, in the Appendix, we describe properties of each radio source individually.

We adopt a radio spectral index $\alpha = 0.8$ ($S_\nu \propto \nu^{-\alpha}$), unless a spectral index could be calculated using the 1.4 GHz, 610 MHz and 325 MHz data. We assume throughout a low-density, Λ-dominated Universe in which $H_0 = 70$ km s^{-1}Mpc^{-1}, $\Omega_{\rm M} = 0.3$ and $\Omega_\Lambda = 0.7$.

2 DATA AND OBSERVATIONS

Optical and X-ray observations of the SXDF (Fig. 1) were made within the 1.3 square degree Subaru/*XMM-Newton* Deep Field with Subaru and *XMM-Newton* respectively. A follow-up deep radio imaging survey at 1.4 GHz was conducted with the Very Large Array (VLA) in B and C configurations (Simpson et al. 2006). A-array observations are also available (Ivison et al. 2007). The total radio catalogue, hereafter the SXDS, covers 0.8 deg^2 to a peak flux density limit of 100 μJy at 1.4 GHz.

The Subaru–XMM-Newton Deep Field (SXDF) has excellent multi-wavelength coverage, having been observed in X-rays with the XMM-Newton satellite (Ueda et al., in prep.), in the optical $BVRi'z'$ bands with Suprime-Cam on the Subaru telescope (Sekiguchi 2004), in the near infrared J and K bands as part of the UKIRT Infrared Deep Sky Survey Ultra-Deep Survey (UKIDSS - UDS; Lawrence et al. 2007), in all of the Spitzer IRAC (3.6, 4.5, 5.8 and 8.0 μm) and MIPS (24, 70 and 160 μm) bands as part of the Spitzer Wide-area Infra-Red Extragalactic (SWIRE) survey Lonsdale et al. (2003) and at sub-mm wavelengths (450 μm and 850 μm; Mortier et al. 2006 & Aretxaga et al. 2007). The area is large (for such a deep survey), at approximately 1 square degree in the optical and near-infrared, although the coverage varies between the different wavebands. The UDS covers approximately 0.8 deg^2 centred on the SXDF.

We study here the brightest 37 radio sources from the 1.4 GHz SXDS (Simpson et al. 2006); these are named, hereafter, sxds_0001 to sxds_0037 in decreasing order of 1.4-GHz flux density. Table 1 gives basic information about our sample, like their radio position, flux density, redshift, optical and radio classification, spectral index, angular size and K (2.2 μm) magnitude (in the AB magnitude system). We adopt the radio structure classification from Owen & Laing (1989), using the VLA data to classify objects as CD, TJ, FD or COM (compact) radio sources. Wherever available, we used the A-array data to determine whether an object has compact hotspots and is therefore a 'CD': in the few cases where this classification

is uncertain, because of no available A-array data, we took our best guess based on the appearance of the B-array map and marked the classification with a '?'. Details of the optical classification are presented in Section 3.3.

In Table 2 we give the result of optical spectroscopy of the SXDS radio sources. We have $\approx 65\%$ (24 out of 37) completeness in spectroscopic redshifts, with the spectra shown in Fig. A1. Table 2 summarises spectroscopic observations carried out on the SXDS objects using either the ISIS spectrograph on the WHT telescope, FOCAS on the SUBARU, 2dF or AAOmega on the AAT, VIMOS on the ESO-VLT, SITe1 on the Magellan 2 or DEIMOS on the Keck 2. Calculation of redshifts from VIMOS spectra were done by using the *fxcor* cross-correlation task in IRAF with SDSS galaxy templates (Simpson et al. in prep), apart from sxds_0025 where the cross-correlation failed (see Appendix A). FOCAS spectra have been corrected for atmospheric absorption. The object sxds_0016 has spectroscopy obtained with the DEep Imaging Multi-Object Spectrograph (DEIMOS) on the Keck 2 telescope (van Breukelen et al. 2007).

Table 3 presents the blueness and mid-IR excess, the radio luminosity at 1.4 GHz $L_{1.4{\rm GHz}}$, the luminosity at 24 μm $[\lambda L]_{24\mu{\rm m}}$ and basic quantities for the SXDS radio sources used in the analysis (see Sec. 4.1).

Optical and infrared photometric data were used to create SEDs for our objects as shown in Fig. A1. Thirteen of our objects are not as yet spectroscopically confirmed, so we use photometric redshifts for our analysis (Sec. 3.2). In Figure 1 we have shown the sky area occupied by the 37 radio sources in our sample. We are confident that our sample is fairly complete. A NVSS-selected 2-mJy sample in the same area gets 34 of the 37 SXDS sources, and the other four lie just below the formal NVSS 2.3 mJy flux density limit.

In order to calculate spectral indices for our sample we use either the 325 MHz catalogue of Tasse et al. (2006), or the 610 MHz flux densities from Ibar et al. (in prep), taking into account the radio-source structure from the A/B-array maps.

Tasse et al. (2006) surveyed the XMM-LSS field (Pierre et al. 2004) in A- and B-array VLA configurations at 325 MHz (see Sec. 6). To minimise the effect of Doppler-boosted emission, we would ideally have selected our objects at 325 MHz, but this survey was unavailable at the time the selection was made. We have, however, subsequently cross-matched the 325 MHz sample with the whole 1.4 GHz radio catalogue. The resolution of the 325 MHz data is 6.7 arcsec and it has a median 5σ sensitivity of 4 mJy beam^{-1}. Figure 1 shows the 325-MHz sources that are in a sky area somewhat larger than our SXDS sample. From our 37-source sample only 22 match with the 325 MHz catalogue. For all of the matching objects we calculate radio spectral indices using the 1.4 GHz and 325 MHz
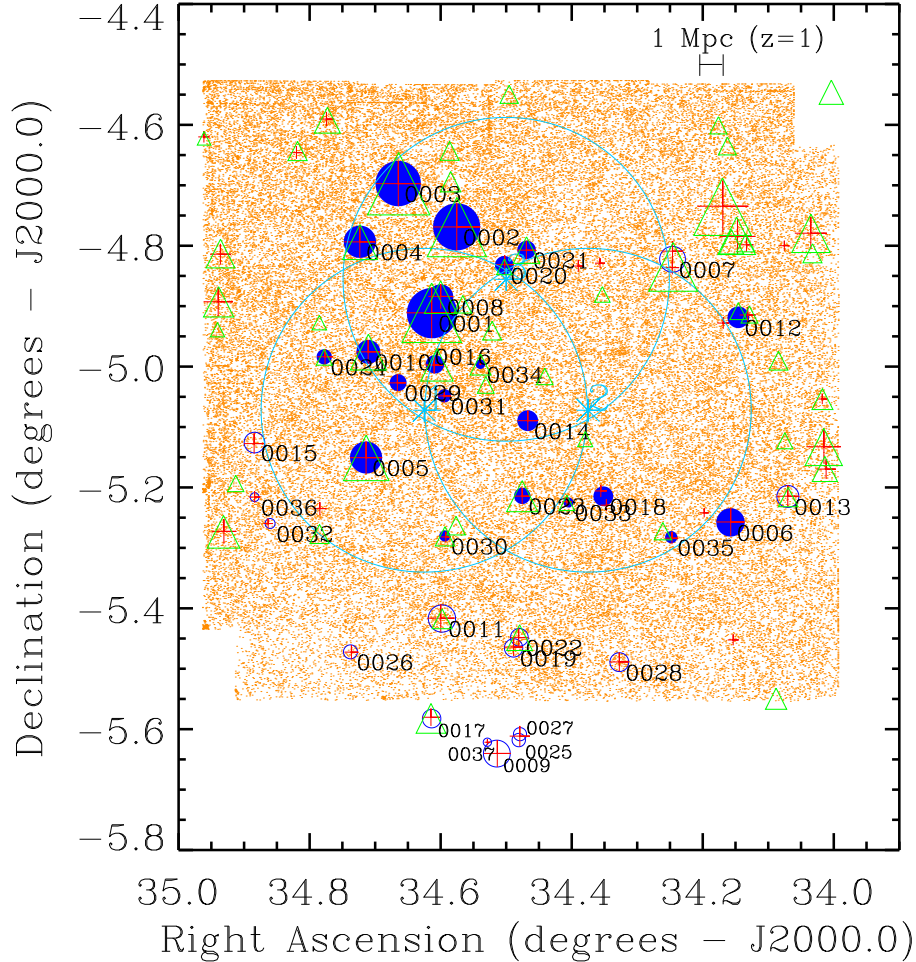
Figure 1. Sky positions of the 37 brightest radio sources in the SXDS (blue circles); these are scaled by the logarithm of the integrated flux density at 1.4 GHz from the VLA observations of Simpson et al. (2006) starting at $S_{1.4\mathrm{GHz}} = 2$ mJy. The shaded area shows the UKIDSS-UDS (Lawrence et al. 2007) coverage. Note that sxds_0009, sxds_0017, sxds_0025, sxds_0027 and sxds_0037 lie outside the UDS coverage. Light-blue stars are the VLA A-array pointing positions and big light-blue circles the FWHM points of the primary beam of the VLA primary beam; objects inside these regions have reasonable quality A-array maps and are highlighted with filled blue circles. Green triangles are the 325 MHz sources ($S_{325\mathrm{MHz}} \gtrsim 4$ mJy) in this area (Tasse et al. 2006). Red crosses are NVSS (Condon et al. 1998) sources in the same sky area, again with the symbol size scaled by the logarithm of the NVSS flux density starting at 2 mJy. The 1 Mpc bar shows the proper physical size of a 1 Mpc-long ruler at $z = 1$.

flux densities. Limits on the spectral indices are calculated assuming a $S_{325\mathrm{MHz}} \lesssim 4$ mJy (5σ) limit for the 325 MHz catalogue, although (see Appendix A) there are a few cases where this process is unreliable (e.g. sxds_0011 where a steep spectral index is expected from the TJ radio structure of this radio source).

The fact that there are 13 325-MHz objects with reasonably high flux density that match with lower 1.4-GHz flux density objects than our 2 mJy limit is unsurprising, given that $S_{325\mathrm{MHz}} \gtrsim 4$ mJy corresponds to $S_{1.4\mathrm{GHz}} \lesssim 2$ mJy for $\alpha \sim 0.9$ and such steep-spectrum objects exist; their number will be exaggerated by random biases on the 325-MHz flux densities at the limit of the Tasse et al. (2006) survey.

The 610-MHz observations of the SXDF were made with the Giant Metre-wave Radio Telescope

(GMRT) in two observing runs: on 2006 February 2–5 and 2006 December 4–9 (details can be found in Ibar et al. in prep). The region was covered with three pointings forming an equilateral triangle with 22-arcmin sides, covering an area of $\sim$0.5 deg^2. Adding both sets of observations, the total integration time per pointing was 11.4 hr.

To calibrate the data, we used 3C 147 or 3C 48 as flux and bandpass calibrators, observed for 20 min at the beginning and end of each track. We also observed 0116−208 or 0240−231 for 7 min every 45 min to be used as phase and amplitude calibrators. The full available bandwidth of 32 MHz was split into two intermediate frequencies (IFs) of 128 channels each, and reduced independently.

For the data reduction we used the Astronomi-

cal Image Processing System (AIPS). Standard tasks (e.g. QUACK, TVFLG, UVFLG, SPFLG) were used to flag bad baselines, antennas, initial integrations, and channels that suffered from narrow-band interference. A first rough calibration using CALIB and CLCAL was performed before using the FLGIT task to flag more bad data using a noise-based criterion. The clean data were calibrated again and used to normalise the target using GETJY. Each IF was compressed in chunks of 7 channels (to ensure bandwidth smearing was not a problem) leaving 15 averaged channels which were used for imaging. Each pointing was broken into 37 facets, in order to minimise 3D non-coplanar issues, and imaged using IMAGR.

The GMRT has a large number of antennas in the central region. These dominate the *uv* coverage and result in a non-Gaussian beam shape. Baselines shorter than 1.5 kλ were omitted from the imaging. We utilised one self-calibration in phase and two in phase and amplitude, averaging both polarisations in these two last passes, in order to obtain the final image facets. These were combined using FLATN, after convolving them to a single, common beam size. The final radio image reaches an r.m.s. of ~ 60 μJy beam^{-1} near the centre of the field, with a synthesised beam of 6.8×5.4 arcsec^2 at position angle of 30 deg. The south-west field, centred at R.A. 2h 18m 44.0s, Dec. -5° $7'$ $20''$ has a considerably larger mean r.m.s. ($\sim 100\mu$Jy) than the other two fields. Also, the noise in the image increases near bright sources, where it can be as high as ~ 300 μJy r.m.s., limiting the detection of nearby sources.

3   ANALYSIS

3.1   Basic information

In our analysis we use the radio flux densities from Table 1 according to the following criteria. In the cases where the NVSS flux density is higher than the SXDS one, and the source is not compact, we use the NVSS flux density for our analysis, since the source may have more structure than the B-configuration VLA observations could reveal. On the other hand, when the NVSS flux density is higher than the SXDS flux density and the source is compact we assume that the NVSS measurement is inaccurate due to confusion by a nearby source (which we confirmed by inspection of the VLA image); in this case we use the SXDS flux density. Finally, when the SXDS flux density is higher than the NVSS value, and the source has compact radio structure, we assume that the source is time variable; in that case we also use the SXDS flux density for our analysis.

For every SXDS radio source $K-$band UDS images were downloaded from the WFCAM archive (Hambly et al. 2007), with the exception of sxds_0009, sxds_0017, sxds_ 0025, sxds_0027 and sxds_0037 that

Table 1. Basic properties of the 37 brightest SXDS radio sources; values in bold are those used in the analysis. **Columns 1, 2 & 3** give the name of the object and its VLA (1.4 GHz) radio position (J2000.0) from Simpson et al. (2006). **Columns 4 & 5** give the integrated flux densities at 1.4 GHz from Simpson et al. (2006) and NVSS respectively; radio sources labelled with 'x' suffer from confusion by a nearby source, which results in a higher NVSS flux density than the SXDS value as seen in objects sxds_0025 and sxds_0027. Objects sxds_0034, sxds_0036 and sxds_0037 are not in the NVSS catalogue since they are fainter than the 2.3 mJy limit of the survey (Condon et al. 1998); their flux densities were measured from the NVSS maps and are labelled with 'n'. **Column 6** gives the 610 MHz flux density in mJy (Ibar et al. in prep); the character 's' shows that the flux densities of each component of the radio source have been added to calculate the whole flux density of the radio sources; '(nif)' means that the object is not inside the field that was observed; values in brackets are inaccurate since they miss part of flux density coming from the source. In **Column 7** we give the 325-MHz flux density from Tasse et al. (2006); values in brackets are not accurate since they miss part of the flux density coming from the source. **Column 8** shows our radio source counterpart optical/IR classification (see Sec. 3.3): 'Q' stands for a quasar, 'OQ' for an obscured quasar, 'G?' for a possible galaxy, 'G' for a secure galaxy, 'SB' for a starburst, 'WQ' for a weak quasar and 'BL' for a BL Lac object. **Column 9** gives the spectroscopic redshift, when available: '?' denotes objects with spectroscopy yielding plausible but insecure redshifts; the symbol '+' indicates clear broad emission lines and 'a' denotes a broad-absorption-line QSO (BALQSO). **Columns 10 & 11** give the photometric redshift calculated with HYPERz using Coleman (CWW) and Bruzual-Charlot (BC) templates respectively; brackets are used to denote unreliable fits. **Column 12** gives the radio spectral index from 1.4 GHz to 610 MHz or from 1.4 GHz to 325 MHz, which are marked with 'm'; we use the 1.4 GHz flux densities in bold for the calculations. Estimated values are in brackets. **Column 13** gives the largest angular size in units of arcsec and **Column 14** gives the radio classification (R Cl) of each object (Owen & Laing 1989): CD stands for classical double; TJ for twin-jet; FD for fat double; and COM for a compact radio source.

were not observed by the UDS (Fig. 1). For these objects we use $z-$band images from Subaru in order to produce overlays of the radio B-array VLA data and imaging, as shown in Fig. A1. Also in Fig. A1 we present spectral energy distributions (SEDs) of the objects created as explained in Section 3.2.

(1)	(2)	(3)	(4)	(5)	(6)	(7)	(8)	(9)	(10)	(11)	(12)	(13)	(14)
Name	RA (h m s)	Dec (° ′ ″)	$S_{\rm SXDS}$ int (mJy)	$S_{\rm NVSS}$ int (mJy)	S_{610MHz} int (mJy)	S_{325MHz} int (mJy)	Optical/IR Type	z_{spec}	z_{phot} CWW	z_{phot} BC	α	θ (arcsec)	R Cl
sxds_0001	02 18 27.32	-04 54 37.29	80.25	**82.5**	194.4	183.5	G	**0.626**	0.618	0.710	1.03	30	TJ
sxds_0002	02 18 18.16	-04 46 07.23	**62.11**	61.8	135.0	180.6	OQ	**1.183**	1.080	1.020	0.93	4.4	CD
sxds_0003	02 18 39.53	-04 41 50.10	50.82	**53.6**	141.3	236.7	OQ	**2.433**	[2.044]	[1.445]	1.17	9	CD
sxds_0004	02 18 53.64	-04 47 35.09	**16.95**	15.1	22.4	21.5	BL	?	[2.126]	**2.270**	0.34	<2	COM
sxds_0005	02 18 51.34	-05 09 00.60	**16.01**	16.7	38.8	53.9	G?	?	1.633	**1.610**	1.07	<2	COM
sxds_0006	02 16 37.86	-05 15 28.15	**12.02**	11.2	7.0	−	G?	−	1.650	**1.882**	-0.65	<2	COM
sxds_0007	02 16 59.02	-04 49 20.53	**9.60**	9.2	43.3^s	71.0	G?	**1.325?**	[1.174]	0.980	1.81	123	CD
sxds_0008	02 18 23.99	-04 53 04.10	**9.15**	8.7	16.6	17.5	SB	**0.458**	[0.218]	0.500	0.72	<2	COM
sxds_0009	02 18 03.37	-05 38 25.00	**8.91**	10.5^x	(nif)	19.3	Q?	**3.570?**	[3.565]	3.585	0.53	2.5	COM
sxds_0010	02 18 50.55	-04 58 32.00	**8.12**	7.9	17.1	23.0	G?	−	[1.231]	**1.400**	0.90	3.3	COM?
sxds_0011	02 18 23.52	-05 25 00.44	7.95	**10.9**	13.3	5.7	G	**0.647**	0.618	0.695	(0.8)	120	TJ
sxds_0012	02 16 34.99	-04 55 05.61	6.59	**6.9**	15.4	(4.4)	G	**0.865**	0.868	0.770	0.97	120	CD
sxds_0013	02 16 16.82	-05 12 53.47	**6.25**	6.9	6.7	5.4	Q	**2.713^{+a}**	[2.922]	[2.475]	0.08	<2	COM
sxds_0014	02 17 52.14	-05 05 21.25	**6.19**	5.7	4.2	−	G?	?	[0.240]	**2.205**	-0.47	<2	COM
sxds_0015	02 19 32.20	-05 07 32.66	**6.10**	6.0	17.0^s	−	G	**0.344**	0.386	0.385	1.23	47	FD
sxds_0016	02 18 26.12	-04 59 46.57	**5.95**	4.4	14.1^s	16.9	OQ	**1.345?**	1.008	1.082	1.04	45	CD
sxds_0017	02 18 27.57	-05 34 53.77	**4.97**	4.6	(nif)	13.5	Q	**2.583^{+a}**	[2.771]	[2.120]	0.68^m	22	CD?
sxds_0018	02 17 24.38	-05 12 51.68	4.84	**5.7**	13.3	−	G	**0.919**	0.858	0.820	1.02	100	FD
sxds_0019	02 17 57.26	-05 27 55.82	4.83	**5.0**	(nif)	−	G	**0.694**	[2.071]	0.910	(0.8)	52	FD?
sxds_0020	02 18 00.68	-04 49 54.78	4.60	**5.1**	8.5^s	3.9	G?	−	[2.553]	**1.135**	0.62	35	FD?
sxds_0021	02 17 52.53	-04 48 23.90	**4.42**	5.0^x	9.1	10.2	G?	−	1.728	**1.645**	0.87	<2	COM
sxds_0022	02 17 55.15	-05 26 52.99	**4.36**	4.7^x	6.1	9.5	G	**0.248**	0.280	0.290	0.40	<2	COM
sxds_0023	02 17 54.10	-05 12 49.94	**4.20**	4.1	11.3	15.2	G	**0.586**	0.561	0.610	1.19	3	COM
sxds_0024	02 19 06.64	-04 59 00.56	3.61	**3.8**	11.2	4.02	G	**0.516**	0.459	0.500	1.30	45	TJ
sxds_0025	02 17 55.42	-05 37 04.97	**3.23**	5.9^x	(nif)	−	WQ?	**0.964?**	[0.019]	[2.465]	(0.4)	<2	COM
sxds_0026	02 18 57.04	-05 28 19.98	3.20	**3.4**	6.4	−	G	**0.450**	0.430	0.445	0.76	10	TJ?
sxds_0027	02 17 54.93	-05 36 29.10	**3.13**	5.9^x	(nif)	−	OQ?	?	[0.011]	**1.595**	(0.4)	<2	COM
sxds_0028	02 17 18.59	-05 29 21.02	**2.80**	5.2^x	4.1	−	G	**0.627?**	[1.092]	0.895	0.46	<2	COM
sxds_0029	02 18 39.58	-05 01 34.68	**2.72**	4.4^x	3.4	−	G?	−	1.272	**1.380**	0.27	<2	COM
sxds_0030	02 18 22.44	-05 16 48.77	**2.56**	2.4	4.6	5.4	G	**0.535**	0.511	0.650	0.71	4	TJ?
sxds_0031	02 18 22.65	-05 02 53.26	2.44	**3.2**	3.9	−	G?	−	1.335	**1.325**	0.24	<2	COM
sxds_0032	02 19 26.48	-05 15 35.00	**2.39**	2.3	7.7^s	−	G	−	1.196	**1.010**	1.41	15	FD?
sxds_0033	02 17 37.21	-05 13 27.96	2.37	**2.4**	6.3	3.9	G	**0.647**	0.774	0.790	1.16	18	TJ
sxds_0034	02 18 09.48	-04 59 45.54	**2.31**	1.21^n	4.2	6.2	OQ	**1.095**	[1.309]	[1.345]	0.72	<2	COM?
sxds_0035	02 16 59.52	-05 16 55.73	**2.24**	2.9^x	1.5	−	G?	−	3.144	**2.715**	-0.48	<2	COM
sxds_0036	02 19 32.15	-05 12 57.26	**2.09**	2.72^n	<1.1	−	G	**0.871**	0.857	0.840	<-0.77	<2	COM
sxds_0037	02 18 06.88	-05 37 17.67	**2.07**	1.68^n	(nif)	−	G?	−	[0.709]	**1.085**	(0.4)	<2	COM

Table 2. Observing log for optical spectroscopy of the SXDS radio sources: **Column 1** gives the name of the object. **Column 2** gives the optical position of the radio sources in RA (h m s) and DEC (° m s). **Column 3** shows the instrument and telescope where spectroscopic observations were conducted; either with ISIS at the WHT (*www.ing.ias.es*), with FOCAS at the SUBARU (*www.subarutelescope.org*), with VIMOS at the ESO-VLT (*www.eso.org/instruments/vimos/*), with 2dF/AAOmega at the AAT (*www.aao.gov.au/AAO/*), with SITe1 at the Magellan 2 (*www.ociw.edu/Magellan*), or with DEIMOS at Keck 2 (*www.keckobservatory.org*). **Column 4** gives the observing date and **Column 5** the spectroscopic redshift (a '?' is added when the redshift not reliable). **Column 6** gives the exposure time; in the case of the WHT we give exposure time for both the ('B') and ('R') parts of the spectrum.

(1)	(2)	(3)	(4)	(5)	(6)
Object	Optical position	Spectrometer/Telescope	Date	$z_{\rm spec}$	Exposure Time (s)
sxds_0001	02 18 27.161	VIMOS/ESO-VLT	26Oct2005	0.626	5400
	-04 54 41.60	ISIS/WHT	26Jul2003	0.625	1x900B, 2x900R
sxds_0002	02 18 18.139	ISIS-WHT	26Jul2003	1.183	1x1800B, 2x900R
	-04 46 07.55				
sxds_0003	02 18 39.559	VIMOS/ESO-VLT	28Oct2005	2.432	5400
	-04 41 49.57	ISIS/WHT	26Jul2003	2.433	1x1800B, 2x900R
sxds_0004	02 18 53.587	AAOMEGA/AAT		?	1800
	-04 47 36.29				
sxds_0005	02 18 51.326	ISIS/WHT	27Jul2003	?	1x1800B, 2x900R
sxds_0006	02 16 37.825				
	-05 15 28.28				
sxds_0007	02 16 59.064	FOCAS/SUBARU	22Dec2003	1.325	1200
	-04 49 20.85				
sxds_0008	02 18 24.005	2dF/AAT	7Dec2002	0.457	1800
	-04 53 05.23	VIMOS/ESO-VLT	26Oct2005	0.458	5400
sxds_0009	02 18 03.420	AAOMEGA/AAT		3.570?	1800
	-05 38 25.43				
sxds_0010	02 18 50.491				
	-04 58 32.31				
sxds_0011	02 18 23.532	2dF/AAT	7Dec2002	0.647	1800
	-05 25 00.69	SITe1/Magellan 2	18Oct2003	0.647	2280
sxds_0012	02 16 34.968	VIMOS/ESO-VLT	8Aug2005	0.865	5400
	-04 55 06.47				
sxds_0013	02 16 16.822	FOCAS/SUBARU	6Oct2003	2.713	1800
	-05 12 53.71				
sxds_0014	02 17 52.118	AAOMEGA/AAT		?	1800
	-05 05 22.23				
sxds_0015	02 19 32.201	2dF/AAT	12Dec2002	0.344	1800
	-05 07 32.67	AAOMEGA/AAT		0.344	1800
sxds_0016	02 18 26.116	DEIMOS/KECK 2	21Dec2006	1.345?	
	-04 59 46.57				
sxds_0017	02 18 27.312	FOCAS/SUBARU	23Dec2003	2.583	1800
	-05 34 57.40				
sxds_0018	02 17 24.415	FOCAS/SUBARU	28Oct2003	0.919	1800
	-05 12 52.63				
sxds_0019	02 17 57.288	FOCAS/SUBARU	20Dec2003	0.694	1800
	-05 27 55.88				
sxds_0020	02 18 00.716				
	-04 49 56.41				
sxds_0021	02 17 52.531				
	-04 48 24.68				
sxds_0022	02 18 18.139	VIMOS/ESO-VLT	2Sep2005	0.248	5400
	-04 46 07.55				
sxds_0023	02 17 54.125	VIMOS/ESO-VLT	8Oct2005	0.586	5400
	-05 12 50.14				
sxds_0024	02 19 06.665	VIMOS/ESO-VLT	10Oct2005	0.516	5400
	-04 59 01.78				

Table 2. (continued)

(1)	(2)	(3)	(4)	(5)	(6)
Object	Optical position	Spectrometer/Telescope	Date	$z_{\rm spec}$	Exposure Time (s)
sxds_0025	02 17 55.392	VIMOS/ESO-VLT	7Oct2005	0.936?	5400
	-05 37 05.00				
sxds_0026	02 18 57.046	2dF/AAT	8Dec2002	0.450	1200
	-05 28 19.38	2dF/AAT	10Dec2002	0.450	1200
sxds_0027	02 17 54.943	VIMOS/ESO-VLT	7Oct2005	?	5400
	-05 36 29.80				
sxds_0028	02 17 18.564	FOCAS/Subaru	25Dec2003	0.627?	1200
	-05 29 20.71				
sxds_0029	02 18 39.586				
	-05 01 35.63				
sxds_0030	02 18 22.493	AAOMEGA/AAT	31Aug2006	0.535	1800
	-05 16 48.83				
sxds_0031	02 18 22.620				
	-05 02 53.77				
sxds_0032	02 19 26.484				
	-05 15 34.62				
sxds_0033	02 17 37.198	2dF/AAT	10Dec2002	0.647	1800
	-05 13 29.58	SITe1/Magellan 2	11Mar2005	0.647	2400
sxds_0034	02 18 09.456	FOCAS/SUBARU	18Dec2003	1.095	1200
	-04 59 45.89				
sxds_0035	02 16 59.546				
	-05 16 56.32				
sxds_0036	02 19 32.143	FOCAS/Subaru	20Dec2003	0.871	1200
	-05 12 57.64				
sxds_0037	02 18 06.893				
	-05 37 17.88				

Table 3. Column 1 gives the name of the object. **Columns 2 & 3** are the blue excess $(\log_{10}([\nu L]_{4000\mathring{A}\text{rest}}/[\nu L]_{1\mu\text{mrest}}))$ and the mid-IR excess $(\log_{10}([\nu L]_{10\mu\text{mrest}}/[\nu L]_{1\mu\text{mrest}}))$ respectively. **Columns 4 & 5** give the logarithms of the rest frame luminosity at 1.4 GHz and at 24 μm respectively. **Column 6** is the K_{AB} magnitude from the UDS; the character 'K' denotes point sources at the $K-$band, whereas 'o' denotes point sources in the optical. For sxds_0009, sxds_0017, sxds_0025, sxds_0027 and sxds_0037 we give an estimate of the K magnitude from the SED of the object (see Fig.1); these values are in brackets.

(1)	(2)	(3)	(4)	(5)	(6)
Object	Blueness	mid-IR excess	$\log_{10}($ $L_{1.4\text{GHz}}/$	$\log_{10}($ $[\lambda L]_{24\mu\text{m}}/$	K_{AB}
			$[\text{WHz}^{-1}\text{sr}^{-1}])$	$[\text{W}])$	(mag)
sxds_0001	-1.17	< -1.40	25.04	< 36.88	18.49
sxds_0002	-0.60	-0.71	25.57	37.30	19.93
sxds_0003	0.33	< 0.58	26.39	37.98	20.89
sxds_0004	-0.17	0.88	25.38	38.04	21.40^K
sxds_0005	-0.32	< 0.04	25.36	< 37.72	20.57
sxds_0006	-1.23	< 0.17	24.62	< 38.16	20.21
sxds_0007	-0.60	< -0.58	25.20	< 37.64	19.68
sxds_0008	-0.21	-0.13	23.71	37.34	18.24
sxds_0009	-0.96	< 0.19	25.61	< 38.51	$(22.52)^o$
sxds_0010	-0.76	< -0.39	24.85	< 37.60	21.11
sxds_0011	-0.89	< -1.51	< 24.15	< 36.89	18.07
sxds_0012	-1.01	< -1.31	24.29	< 37.08	19.11
sxds_0013	-0.36	< 0.73	24.96	< 38.25	21.79^o
sxds_0014	-3.19	< -2.25	24.51	< 38.33	21.23^K
sxds_0015	-0.33	-0.85	23.31	36.66	17.69
sxds_0016	-0.49	< -0.19	24.73	37.86	22.06
sxds_0017	0.30	< 1.07	25.15	< 38.15	$(21.64)^o$
sxds_0018	-0.78	< -1.22	24.29	< 37.18	18.88
sxds_0019	-0.54	< -0.57	< 23.88	< 36.97	20.26
sxds_0020	0.06	0.60	24.33	< 37.43	21.22
sxds_0021	-0.09	< 0.54	24.80	< 37.72	21.04
sxds_0022	-0.54	-1.54	22.76	35.87	16.48
sxds_0023	-0.42	< -1.02	23.71	< 36.71	18.97
sxds_0024	-0.82	< -1.63	23.55	< 36.66	17.80
sxds_0025	0.09	< 0.57	< 23.91	< 37.29	(21.60)
sxds_0026	-1.00	< -1.74	23.27	< 36.54	17.65
sxds_0027	-0.39	0.81	< 24.37	38.38	(20.72)
sxds_0028	-0.27	< -0.69	23.45	< 36.84	18.71
sxds_0029	-0.91	< -0.65	24.12	< 37.63	20.62
sxds_0030	-0.85	< -1.23	23.31	< 36.65	18.44
sxds_0031	-0.78	< -0.21	24.15	< 37.58	20.32
sxds_0032	-0.47	< -0.22	24.13	< 37.27	20.51
sxds_0033	-0.23	-1.02	23.57	36.83	18.40
sxds_0034	-0.08	1.00	24.00	38.60	19.75^{Ko}
sxds_0035	-0.80	< 1.50	24.19	< 38.28	21.86
sxds_0036	-1.36	< -1.32	< 23.31	< 37.08	18.71
sxds_0037	-0.92	< -0.52	< 23.83	< 37.40	(20.60)

Table 4. Approximate 5-σ point-source depths for the bands used in the SXDF, and, for the Spitzer bands, the flux density limits of the SWIRE catalogues (used as upper limits in the SEDs for undetected objects).

Band	Depth		Catalogue flux limit
	AB mags	μJy	μJy
B	27.5	3.6×10^{-2}	—
V	26.7	7.6×10^{-2}	—
R	26.8	6.9×10^{-2}	—
i'	26.5	9.1×10^{-2}	—
z'	25.5	0.23	—
J	23.5	1.4	—
K	23.5	1.4	—
3.6 μm	22.5	3.7	10
4.5 μm	22.1	5.4	10
5.8 μm	19.7	48	43
8.0 μm	20.0	37.8	40
24 μm	18.0	230	450

3.2 Photometric redshifts

We have estimated redshifts for the objects by fitting template spectral energy distributions - SEDs to their observed photometry, using a modified version of the publicly-available[†] HYPERz code, by Bolzonella et al. (2000). HYPERz offers a convenient interface for the provision of photometric bandpass functions, galaxy templates and data, and is well documented. It also has built-in prescriptions for reddening of templates by dust, and for Lyman forest absorption below 912 Å.

For the purposes of galaxy template fitting, we consider only the optical (Subaru), near-infrared (UKIDSS-UDS) and mid-infrared (SWIRE) data. The approximate 5-σ point source depths achieved in each waveband are shown in Table 4.

The catalogues contain a variety of adaptive and fixed aperture magnitudes, which have been measured from the image data using SExtractor (Bertin & Arnouts 1996). For the purpose of SED fitting, it was important to select those apertures which provided the most accurate colour information for each object. Whilst the adaptive (such as Kron and isophotal) magnitudes provide a good estimate of the total flux of an object (without the need for an aperture correction to be derived based upon the galaxy's assumed surface brightness distribution and the seeing, as is required to correct a small fixed aperture), the apertures must generally be large, containing areas of low surface brightness which increase the photometric error. Also, an adaptive aperture might be a different size in each measured band and thus sample a different component of the stellar population, poten-

tially leading to unphysical colours. For these reasons, and because of the problems using adaptive apertures at faint magnitudes (where errors in determining the correct isophotal or Kron radii can exacerbate photometric errors in low signal-to-noise images), we decided to use fixed aperture photometry for our SED fitting.

However, fixed apertures have their own issues to consider. In the ideal situation, we would have a set of images with the same PSF, perfectly registered astrometrically. It would then be possible to extract photometry using apertures placed in exactly the same positions in each image, and we could be confident that, whatever the aperture size, we would be sampling the same fraction of the light from the same regions of each galaxy studied. But this is far from the case when combining data taken with different instruments, under different seeing conditions, as we are doing here. It was undesirable on confusion grounds to degrade the optical and near-IR data to match the large PSF of the Spitzer bands, so we chose the aperture size to minimise the systematic differences in the fraction of the flux measured in each band.

Clearly, there is a trade-off to be made — too large an aperture is vulnerable to confusion and increased background noise, while an aperture which is very small will contain very different fractions of the total flux for images with different PSFs. To investigate this trade off in detail, we looked at the mean difference between aperture magnitudes and the SExtractor MAG_AUTO magnitudes, which uses an adaptive Kron aperture to estimate the total flux. For the smallest aperture available in all bands (2 arcsec) there were large offsets (of order 0.2–0.3 mags) between the aperture and Kron magnitudes, but most importantly these offsets were very different in the different bands. With the next available aperture diameter (3 arcsec) the mean differences in the aperture and Kron magnitudes were much smaller — less than a tenth of a magnitude. Deeming this an acceptable systematic error, we decided to use 3-arcsec apertures for all photometry.

To combine the catalogues across the optical and infrared bands, we assumed that the closest match between extracted objects, within a search radius of 2 arcsec relative to the radio position (chosen to allow for differences in astrometry between different photometric bands), was the correct association, with the constraint that a catalogue entry was only permitted to match once per band.

We used both empirical and evolving galaxy SEDs in the template fitting. The empirical templates used were the ones supplied with the HYPERz code, which are four typical observed galaxy spectra taken from Coleman, Wu & Weedman (1980; henceforth CWW), extended in the ultraviolet and infrared by matched models (Bruzual & Charlot 1993).

The evolving templates were generated using

[†] webast.ast.obs-mip.fr/hyperz/

GALAXEV (Bruzual & Charlot 2003; henceforth BC[‡]), with 14 exponentially decaying star formation rates with e-folding timescales ranging from 0.1 to 30 Gyr, plus an instantaneous burst, a finite burst and a constant star formation rate template, all with solar metallicity and a Salpeter initial mass function for the stars. This is a larger number of BC templates than used by Bolzonella et al. (2000), but our intention was to span the space of possible galaxy types as finely as possible, in the hope that there would always be a template with similar star formation history to any object in the dataset, and that this would then be the best fit.

Both empirical and evolving SEDs were used because parallel work by van Breukelen et al. (2006) seemed to indicate that, while the evolving templates gave slightly more accurate results on spectroscopically identified (and thus also reasonably bright) samples, they more quickly broke down, giving catastrophic redshift estimates, as signal-to-noise was reduced. Catastrophically wrong redshift estimates produced by the two sets of templates are generally different, so agreement between the results obtained with the CWW and BC SEDs is useful to improve confidence that a particular redshift estimate is correct. Where the estimates differ significantly, it is more often the case that the CWW estimate is closer to reality, though this effect is difficult to quantify precisely since catastrophic redshift estimates are a function of the template set, as well as the precise signal-to-noise in each observed band.

Figure A1 presents the SEDs constructed for our radio sources; red colour represents the BC templates and black the CWW templates. We decided to use the BC derived value in the case where no spectroscopy is available.

In Fig. 2 we compare 24 spectroscopic redshifts with the photometric redshifts (Table 2); optical spectra of these objects are presented in Fig. A1. Note that objects significantly deviating from the $z_{\rm spec} = z_{\rm phot}$ line have unclear photometric redshifts (see Table 1). Three objects in our sample are classified as quasars (see Sec. 3.3), two of which fall into the $z_{\rm spec} > z_{\rm phot}$ category; the third, sxds_0009, may have a good photometric redshift because the tentative broad-line emission could be scattered light, with the nucleus making an insignificant contribution at the longer wavelengths dominating the calculation of the photometric redshift.

The median redshift for our radio-source sample, including photometric redshifts, is $z = 1.095$. The best fit line for the galaxies 'G' gives an excel-
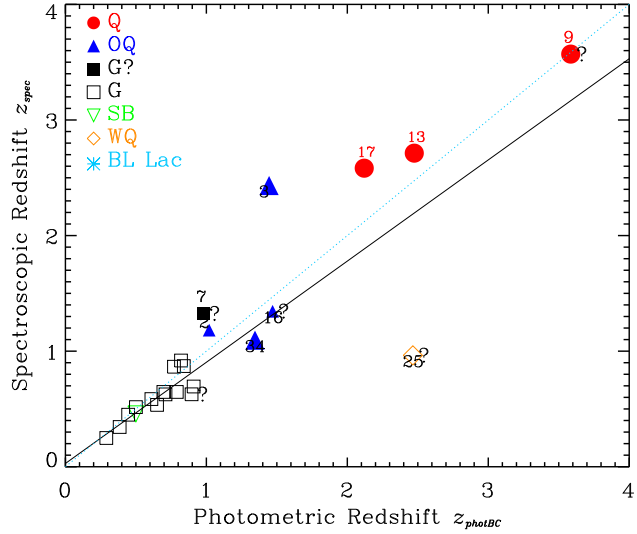
Figure 2. Comparison of spectroscopic and photometric (based on BC templates) redshift in the 24 (of 37) cases where both are available. Symbols indicate optical/near-infrared classification as adopted in Section 3.3, where filled symbols denote objects with spectroscopic redshifts: red filled circles for quasars 'Q', blue filled triangles for obscured quasars 'OQ', black filled squares for possible galaxies 'G?', black squares for secure galaxies 'G', green upside-down triangles for starbursts 'SB', orange diamonds for weak quasars 'WQ' and light-blue stars for 'BL Lac' objects (note that the 'BL' object is not present due to absence of spectroscopic redshift). The light-blue dotted line corresponds to $z_{\rm spec} = z_{\rm photBC}$. The solid black line fits the 15 galaxies 'G' that have both spectroscopic and photometric redshift: $z_{\rm spec-G} = 0.88 \times z_{\rm photBC-G} - 0.03$. Names in red represent objects with broad-line optical features. Outlying points are labelled with their source number. Objects with uncertain photometric redshifts are plotted with symbols, a factor 1.5 larger than the others.

lent agreement between spectroscopic and photometric redshifts, within the errors. The linear Pearson correlation coefficient is 0.89 and the Spearman correlation coefficient is $\rho = 0.96$ with 99.9% probability for a correlation. This makes us confident to use photometric redshifts in the case where no spectroscopy is available. Consequently, we adopt the photometric redshifts in bold-type in Table 1.

3.3 Optical/infrared radio-source classification

Figure 3 shows the rest frame luminosity of the SXDS radio sources at 24 μm versus their redshift. The value of $\log_{10}(L_{24\mu m})$ is calculated using the spectral index measured from the 24 μm data point to the nearest lower-λ detection in the observed frame SED (Fig. A1).

We use optical/IR observations (Fig. 3) to classify a radio source as either Quasar 'Q', Obscured Quasar 'OQ', Galaxy? 'G?', Galaxy 'G', Starburst 'SB', Weak Quasar 'WQ' or BL Lac 'BL', as described

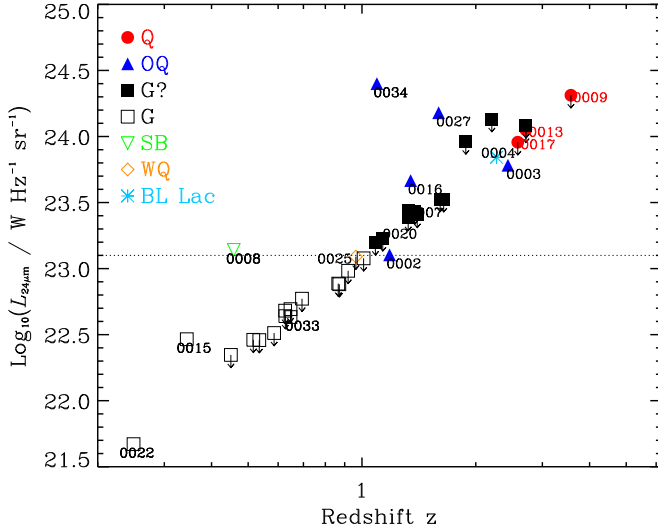**Figure 3.** Logarithm of the rest-frame Luminosity $L_{24\mu m}$ at 24 μm versus redshift z. Symbols are the same as in Fig. 2. The dotted line corresponds to $[\lambda L]_{24\mu m} = 10^{-1.8} L_{\rm Edd}$ for a quasar with $M_{\rm BH} \gtrsim 10^8$ M$_\odot$, as discussed in Section 3.3. Outlying points are labelled with their source number.

below. We deem that nuclear accretion is 'significant' in objects that obey $\log_{10}(L_{24\mu m}/[{\rm WHz}^{-1}{\rm sr}^{-1}]) > 23.1$ (or $[\lambda L]_{24\mu m} > 10^{37.3}$ W)[§]. This value corresponds to $[\lambda L]_{24\mu m} \geq 10^{-1.8} L_{Edd}$, a typical lower limit for quasars at $z \sim 1$ (see Fig. 2 McLure & Dunlop 2004), for a black hole mass $M_{\rm BH} \geq 10^8 M_\odot$, a typical lower limit for radio sources (McLure et al. 2004); $L_{\rm Edd}$ is the Eddington luminosity $L_{Edd} = 10^{39.1} \times (M/10^8 {\rm M}_\odot){\rm W}$.

We then define the following categories:

i) **Q**: Broad lines in the optical spectrum (3/37 cases). None of these are detected at 24 μm, although their limits are insufficient to rule out significant accretion.
ii) **OQ**: Objects with a 24-μm detection (5/37 cases) and with sufficient L_{24} to represent significant accretion. In all cases we believe that the nucleus seen at 24 μm is obscured optically because the spectra show no broad lines. This class may be incomplete in that some objects in the 'G?' class, as described next, have limits above this critical value.
iii) **G?**: A galaxy that has a 24-μm limit consistent with it lying above the $\log_{10}(L_{24\mu m}/ [{\rm WHz}^{-1}{\rm sr}^{-1}]) = 23.1$ line[¶] (11/37 cases).
iv) **G**: All other objects (15/37 cases) without sig-

nificant accretion, unless they fall into three special categories defined by properties derived from considerations of the optical spectroscopy, the SED and the optical structure: **SB**: evidence from the SED and optical spectra of a starburst component (1/37 cases; see notes in Appendix A); **WQ**: evidence from the SED and optical spectra of a quasar component (see notes in Appendix A) but no 24 μm detection (1/37 cases); **BL**: Featureless red continuum and a point source at K (1/37 cases).

Objects labelled as 'Q', 'OQ' and 'G?' include all objects with, or potentially with, significant nuclear accretion, and are represented by filled symbols in Fig. 4. Note, however, that the definition of 'significant' accretion is somewhat arbitrary as illustrated by the case of the 'WQ' sxds_0025. Some accretion may be necessary in many, or perhaps all FRIs, and especially those near the FRI/FRII divide, if the radio luminosity is assumed to be derived from the Blandford-Znajek mechanism (Cao & Rawlings 2004).

4 DISCUSSION

4.1 Accretion Indicators

Inspection of the SEDs in Fig. A1 shows that some of our objects have excess emission at 24 μm above that expected from extrapolation of the stellar populations. This is quantified via a measure of mid-IR excess, $\log_{10}([\nu L]_{10\mu m {\rm rest}}/[\nu L]_{1\mu m {\rm rest}})$ (Table 3). We chose a rest-frame value of 10 μm as our fiducial point as this corresponds to ~ 24 μm in the observed frame for redshifts close to the median redshift of our sample. A comparison of mid-IR excess and blueness is presented in Fig. 4 where a positive correlation is clear. The generalised Spearman correlation calculated using survival analysis statistics ASURV (Lavalley et al. 1992) is 0.636 with a 99.9% probability for a correlation.

Consider a simple model in which blueness is connected to mid-IR excess through the following equations:

$$[\nu L]_{4000{\rm \mathring{A}rest}} = {\rm k}_1 \times [\nu{\rm L}]_{1\mu m {\rm rest}} + {\rm k}_2 \times [\nu{\rm L}]_{10\mu m {\rm rest}} \Rightarrow (1)$$

$$\log_{10}\left(\frac{[\nu L]_{4000{\rm \mathring{A}rest}}}{[\nu L]_{1\mu m {\rm rest}}}\right) =$$

$$\log_{10}({\rm e}) \times \frac{{\rm k}_2}{{\rm k}_1} \times \left(\frac{[\nu{\rm L}]_{10\mu m {\rm rest}}}{[\nu{\rm L}]_{1\mu m {\rm rest}}}\right) + \log_{10}({\rm k}_1)^{\|}, \qquad (2)$$

where k_1 encodes the contribution of the stellar population of a passively evolving galaxy formed at high redshift ($z > 5$), and k_2 the mid-IR-excess parameter that we are looking to calculate for this sample of radio sources. This model assumes that light from the nucleus with intrinsic optical luminosity $L_{\rm opt}$ is i) absorbed by dust and re-emitted in the mid-IR generating luminosity $[\nu L]_{10\mu m {\rm rest}}$ and ii) scattered, gen-

---

[§] Other authors use slightly different values to separate 'luminous' quasars (and broad-line radio galaxies) from objects with lower accretion rates (e.g. Ogle et al. 2006 adopt a value of $[\lambda L]_{15\mu m} \sim 10^{36.9}$ W).

[¶] Because of the 24 μm flux density limit these objects are the high-redshift (and hence, because of the 1.4-GHz flux density limit) high-$L_{1.4{\rm GHz}}$ sub-set of the objects lacking Spitzer 24 μm detections.
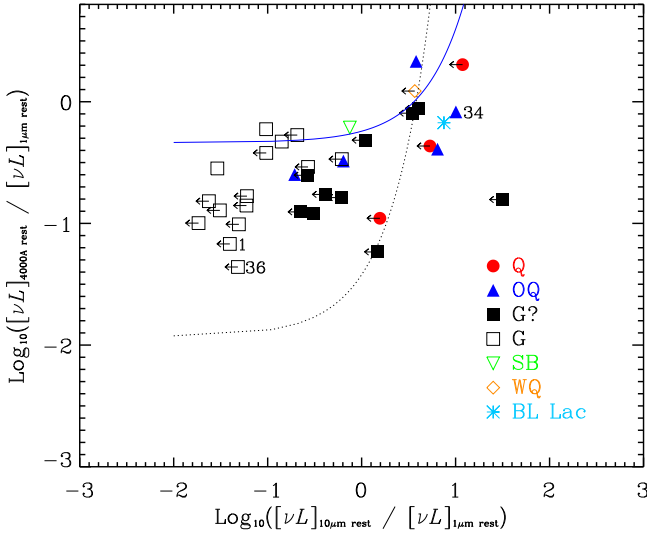
Figure 4. Blueness versus mid-IR excess for the 37 brightest SXDS radio sources: Symbols indicate optical/IR classification, as explained in Fig.2 and Sec. 3.3. Table 3 presents measurements of those quantities. The black dotted line corresponds to the best-fit line in the log-linear plane when all objects were treated as detections; the slope and intercept are 0.51 and -1.93 respectively, giving [see Eqn (2)] $k_1 \simeq 0.01$ and $k_2 \simeq 0.01$. The blue solid line corresponds to the best-fit line in log-linear plane where objects without detections at 24 μm were treated as limits; the slope and intercept are 0.09 and -0.34 respectively, giving $k_1 \simeq 0.46$ and $k_2 \simeq 0.10$. The Buckley-James method in the survival analysis (ASURV) statistics package (Lavalley et al. 1992) was used in these calculations. 'SB', 'BL', 'Q' and 'WQ' objects were excluded from the fits as explained in Sec. 4.1.

erating a contribution to luminosity $[\nu L]_{4000\mathring{\mathrm{A}}\mathrm{rest}}$.

Objects labelled as 'SB', 'BL', 'Q' and 'WQ' have been excluded from the fit since they have SEDs dominated by different physical processes to those assumed in the model described by Eqns (1) and (2). Without spectropolarimetry it is difficult to determine whether any broad lines are seen as scattered light from the nucleus or they represent a direct view of the nucleus. The 24-μm luminosity versus redshift plane of Fig. 3 shows that all three broad-line objects, as well as the 'OQ' objects, are consistent with being above or at the limit of $L_{24\mu m} > 10^{23.1}$ WHz^{-1}sr^{-1}, or $[\lambda L]_{24\mu m} > 10^{37.3}$ W.

Fig. 4 shows best-fit lines for two scenarios: 1) all objects were treated as detections (black dotted line), and 2) objects are treated as upper limits according to their 24 μm detection (blue solid line). We note that these 'fitted' lines are highly sensitive to the locations in the $\log_{10}([\nu L]_{4000\mathring{\mathrm{A}}\mathrm{rest}}/[\nu L]_{1\mu\mathrm{mrest}})$ vs

‖ Equation (2) relies on the $ln(1 + x) \approx x$ approximation which is only accurate around and below the knees of the functions plotted in Fig. 4
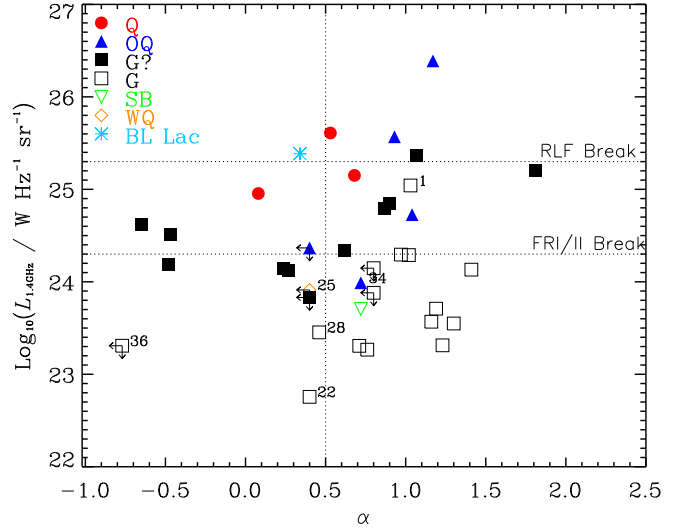

Figure 5. Radio Luminosity at 1.4 GHz $\log_{10}(L_{1.4\mathrm{GHz}}/$ [WHz^{-1}sr^{-1}]) versus the radio spectral index α as in Table 1: symbols are the same as in Fig. 2. The horizontal lines show the RLF and FRI/FRII breaks calculated from the Willott et al. (2003) and the Fanaroff & Riley (1974) values respectively using a typical steep-spectrum spectral index of 0.8. The vertical line at $\alpha = 0.5$ shows the conventional border between steep and flat-spectrum sources. Objects that are discussed in the text (see Sec. 4.1) are labelled with their names.

$\log_{10}([\nu L]_{10\mu\mathrm{mrest}}/[\nu L]_{1\mu\mathrm{mrest}})$ plane of a small number of objects, and hence are not robust, although they certainly seem to delineate rough bounds to the data. Averaging these results we deduce $k_1 \sim 0.2$ and $k_2 \sim 0.06$, which agrees well with independent evidence for the properties of radio sources as we now argue. The value deduced for k_1 is in line with the expectations of template spectra of galaxies which formed their stars at high redshift. Optical polarisation studies (e.g. Kishimoto et al. 2001) tell us that $[\nu L]_{4000\mathring{\mathrm{A}}\mathrm{rest}} \gtrsim 0.01[\nu L]_{\mathrm{opt}}$, which is consistent with our value of k_2 given that QSO SED studies suggest $[\nu L]_{10\mu\mathrm{mrest}} \sim 0.3[\nu L]_{\mathrm{opt}}$ (Rowan-Robinson 1995), and $0.06 \times 0.3 \simeq 0.01$. We conclude that whenever nuclear accretion is significant in our sample of radio sources, dust in the torus absorbs 30% of the photons and dust above and below the torus scatters $\gtrsim 1\%$ of the photons.

In previous studies, the quasar fraction has been defined as the number of sources with quasar-like optical features (e.g. optical broad lines) and has a value of $\sim 0.1 \to 0.4$ over the relevant range of $L_{1.4\mathrm{GHz}}$ (e.g. Willott et al. 2000). We introduce the term 'quasar-mode fraction' f_{QM} to describe the fraction of objects with 'significant' accretion rates, as determined from the observed 24 μm flux density, to the total number of objects.

In Figure 5 we present the radio luminosity at 1.4 GHz of the SXDS radio sources against their radio spectral index α (Table 1). A typical flat/steep-

spectrum radio spectral index $\alpha = 0.4/0.8$, depending on whether its radio structure is compact/extended, was used in the case where the object was not observed at 610 MHz and is a limit at the 325-MHz catalogue. Note that the median radio luminosity is $L_{1.4\text{GHz}} \sim 1.6 \times 10^{24}\,\text{WHz}^{-1}\text{sr}^{-1}$, which lies very close to the FRI/FRII luminosity division. Crudely, the SXDS sample is sensitive to objects above this division at $z \gtrsim 1$ and to objects below the FRI/FRII luminosity break at $z \lesssim 1$.

We see from Fig. 5 that the single 'BL' object has a flat radio spectral index, as expected. It is clear that nearly all the other flat-spectrum object have significant accretion, although some exceptions do exist, e.g. object sxds_0028 lies close to the boundary of $\alpha = 0.5$ although it has significant errors in the calculation of its spectral index. Object sxds_0022 also lies close to the flat/steep α boundary, which is a typical value if star formation is making a significant contribution to the radio flux density (see notes in Appendix A). Object sxds_0025 is a 'WQ' with a flat radio spectra index and is expected to be in that region since we believe we are viewing the central region directly (see notes in Appendix A). The fact that it lies below the limit for 'significant' accretion is consistent with it being a weak quasar. Thus, the only clear exception is sxds_0036, which is a 'G' and there is an uncertainty in the calculation of its spectral index. The only clear region where the quasar-mode fraction is very low, is for steep-spectrum objects below the FRI/FRII break, where $f_{\text{QM}} \sim 0.1$.

Figure 6[**] shows the radio luminosity at 1.4 GHz versus the projected linear size D. For SXDS sources that are compact we assume a limiting angular size $\theta = 2.0$ arcsec (Simpson et al. 2006). We see that nearly all 'Q', 'OQ' and 'G?' objects of our sample lie above the 'FRI/FRII' luminosity break with the exception of the 'OQ' sxds_0034 (the three 'G?' objects near sxds_0034 lie close to the boundary of significant accretion). Above the FRI/FRII break we find that $f_{\text{QM}} \sim 0.5 - 0.9$ (the lower value assumes the 24 μm limits are much higher than the true 24 μm values, whereas the higher value assumes the true values lie just below the limits). The one clear exception in this regime is sxds_0001, which has no evidence of a QSO and a clear Twin-Jet (FRI) radio structure.

The quasar-mode fraction drops dramatically below the FRI/FRII break, and whether or not one excludes some of the compact ($D < 100$ kpc) sources as potentially part of a separate (beamed) population, then $f_{\text{QM}} \lesssim 0.1$ because nearly all objects are galaxies 'G'. The clear counter-example here is sxds_0034, the only 'OQ' below the FRI/FRII break, and potentially an optically-obscured example of unobscured
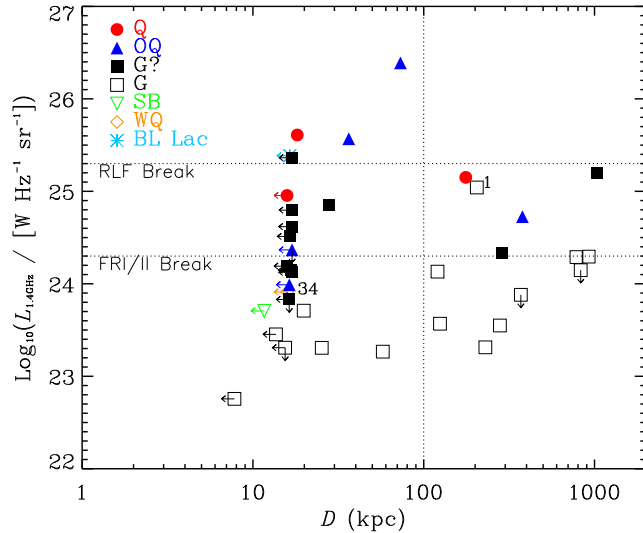
Figure 6. Radio Luminosity at 1.4 GHz $\log_{10}$ ($L_{1.4\text{GHz}}/$ [WHz^{-1}sr^{-1}]) versus largest projected linear size D. Symbols are the same as in Fig. 2. The horizontal lines show the RLF and FRI/FRII breaks calculated from the Willott et al. (2003) and the Fanaroff & Riley (1974) values respectively using a typical steep-spectrum spectral index of 0.8. Objects that are discussed in the text (see Sec. 4.1) are labelled with their names.

FRI QSOs already studied in this radio luminosity regime (e.g. Sarazin et al. 1999, Blundell & Rawlings 2001). This object is spectroscopically confirmed at redshift $z = 1.095$. An excess of emission at 24 μm places it securely in the 'OQ' classification. This object is not a spectroscopically confirmed quasar but has high-excitation narrow lines in its optical spectrum and is compact both optically and at K; its radio map shows a seemingly unresolved source. This seems to be an optically-obscured 'radio-quiet' quasar in the radio luminosity regime in which most radio sources are thought to have FRI radio structures. Unobscured 'radio-quiet' quasars are known in this regime (see Heywood et al. 2007 and references therein), and claims have been made for obscured examples (Martinez-Sansigre et al. 2006). However, as found by the study of Martinez-Sansigre et al. (2006), the surface brightness sensitivity of existing radio data is insufficient to map any extended structure at high redshifts. We also note the presence of broad absorption lines in 2 out of our 3 'Q' category objects. This is a high fraction compared to general QSO samples (e.g. Richards et al. 2003 find this fraction to be between ~ 0.03 and ~ 0.2 for optically selected samples of quasars).

Both of Figs 5 & 6 suggest that we have a larger fraction of flat, compact radio sources in our sample since it is selected at higher frequency than low-frequency selected radio samples like the 3CRR, 6CE and 7CRS: $51\% \pm 7\%$ objects of our sample have $D < 25$ kpc, whereas this fraction is $\sim 25\%$ in 7CRS (e.g. Fig. 18 of Blundell, Rawlings & Willott 1999).

The quasar-mode fraction is generally high for flat-spectrum objects independent of radio luminosity. Steep-spectrum and extended, presumably FRI-type radio sources (i.e. objects below the FRI/II break at $\alpha > 0.5$) show no signs of significant accretion with just one exception. Cao & Rawlings (2004) studied a sample of 3CR FRI radio sources and found that the L/L_{Edd} ratio in FRI-type radio sources is more than two orders of magnitude less than our limit for significant accretion, which is in line with our findings.

We have discovered that above the FRI/FRII division the quasar-mode fraction is of the order $f_{\mathrm{QM}} \sim 1$, where the median redshift of these objects is $z_{\mathrm{med}} \sim 1.6$. Below the FRI/FRII break $f_{\mathrm{QM}} \to 0$ for extended steep-spectrum sources, where $z_{\mathrm{med}} \sim 0.65$. A key question is whether the presence of significant accretion is linked to the radio luminosity L_{rad} (or radio structure) or to the redshift z. We note that from studies of the 3CR sample (in which the FRI/FRII division is at redshift $z \sim 0.1$ rather that $z \sim 1$, for our sample) that a similar division of mid-IR properties occurs at the same FRI/FRII luminosity division (Ogle et al. 2006). We conclude that it is a luminosity (or structural) effect rather than an epoch effect, and in this paper we have shown that such an effect persists from $z \sim 0.1$ to $z \sim 1$. We will attempt to de-couple the effects of radio luminosity and radio structure in a future paper.

5 CONCLUSIONS

We have presented a study of the brightest SXDS radio sources with flux density at 1.4 GHz above 2 mJy. Our sample is not as yet spectroscopically complete (24 out of 37 have spectroscopic redshifts), but Fig.2 gives us the confidence in the use of photometric redshifts calculated with HYPERz using Bruzual-Charlot templates. The median redshift of the entire sample is $z_{\mathrm{med}} \approx 1.1$, which from Fig. 5 corresponds to objects close to the FRI/FRII division. Optical and infrared imaging, as well as radio observations are in place to give an insight to the type of radio sources at the bright flux density end of the 1.4-GHz SXDS radio survey of the SXDF.

We have classified our radio sources as either quasars 'Q', obscured quasars 'OQ', possible galaxies 'G?', secure galaxies 'G', starbursts 'SB', weak quasars 'WQ' or BL Lac objects 'BL'. Objects 'Q', 'OQ' and 'G?' have significant nuclear accretion, since they obey $\log_{10}(L_{24\mu m}/[\mathrm{WHz}^{-1}\mathrm{sr}^{-1}]) > 23.1$ (or $[\lambda L]_{24\mu m} > 10^{37.3}$ W). This value corresponds to $[\lambda L]_{24\mu m} \geq 10^{-1.8} L_{Edd}$ for a black hole mass $M_{\mathrm{BH}} \geq 10^8 M_\odot$.

The 37 brightest radio sources in the SXDS exhibit the following properties:

• Flat-spectrum, presumably mostly Doppler - boosted, radio sources show evidence of accretion in almost all cases, independent of radio luminosity.

• Significant accretion is also nearly ubiquitous above the 'FRI/FRII' luminosity break, i.e. at redshift $z \gtrsim 1$ for objects in our sample. The quasar-mode fraction, defined here as the fraction of objects with significant accretion rates to the total number of objects – and not as the number of sources with quasar-like optical spectra – is $\sim 0.5 \to 0.9$. There are counter examples like the low-accretion FRI sxds_0001, but they are rare.

• At $z \lesssim 1$ most of the 'FRI'-regime sources have low accretion rates and $f_{\mathrm{QM}} \lesssim 0.1$, but one high-accretion-rate object (sxds_0034) does exist; this is an obscured 'radio-quiet quasar' which may have FRI-like jets.

• The presence of significant accretion is linked to the radio luminosity L_{rad} (or radio structure) of the radio source at $z \sim 1$, just as it is at $z \sim 0.1$.

• Mid-IR excess and blueness are correlated, where the Spearman's generalised $\rho = 0.636$ with a 99.9% probability for a correlation.

• This correlation is consistent with a model in which $\sim 30\%$ of the QSO light is absorbed by a dust torus and $\gtrsim 1\%$ is scattered by dust above and below the torus.

Study of the brightest SXDS radio sources in the mid-IR has revealed that the ratio of objects with significant accretion rates to the total number of objects is high for flat-spectrum radio sources, and for steep-spectrum sources above the FRI/FRII radio luminosity divide. This ratio is much lower for objects below the luminosity corresponding to the FRI/FRII divide. Future work on the brightest SXDS radio sources is likely to involve studies of radio structural properties, host galaxies and other indicators of accretion like emission lines and X-rays.

REFERENCES

Antonucci, R., 1993, ARA&A, 31, 473

Aretxaga, I., Hughes, D. H., Coppin, K., Mortier, A. M. J., Wagg, J., Dunlop, J. S., Chapin, E. L., Eales, S. A., Gaztanaga, E., Halpern, M. et al., 2007, MNRAS, 379, 1571

Bertin, E., Arnouts, S., 1996, AAPS, 117, 393

Best, P. N., Kauffmann, G., Heckman, T. M., Brinchmann, J., Charlot, S., Ivezic, Z., White, S. D. M., 2005, MNRAS, 362, 25B

Best, P. N., Arts, J. N., Rttgering, H. J. A., Rengelink, R., Brookes, M. H., Wall, J., 2003, MNRAS, 346, 627

Blundell, K. M., Rawlings, S., 2001, ApJ, 562, 5

Blundell, K. M., Rawlings, S., Willott, C. J., 1999, AJ, 117, 677

Bolzonella, M., Miralles, J. M., Pello, R., 2000, A&A, 363, 476

van Breukelen, C., Cotter, G., Rawlings, S., Readhead, T., Bonfield, D., Clewley, L., Ivison, R., Jarvis, M., Simpson, C., Watson, M., 2007, astro−ph, arXiv : 0708.3838

van Breukelen, C., Clewley, L., Bonfield, D. G., Rawlings, S., Jarvis, M. J., Barr, J. M., Foucaud, S., Almaini, O., Cirasuolo, M., Dalton, G., Dunlop, J. S., Edge, A. C., Hirst, P., McLure, R. J., Page, M. J., Sekiguchi, K., Simpson, C., Smail, I., Watson, M. G., 2006, MNRAS, 373, L26

Bruzual, A. G., Charlot, S., 2003, MNRAS, 344, 1000

Bruzual A. G., Charlot, S., 1993, ApJ, 405, 538

Cao, X., Rawlings, S., 2004, MNRAS, 349, 1419

Cimatti, A., di Serego Alighieri, S., Fosbury, R. A. E., 1993, Salvati, M., Taylor, D., 1993, MNRAS, 264, 421

Coleman, G. D., Wu, C. C., Weedman, D. W., 1980, ApJS , 43, 393

Condon, J. J., Cotton, W. D., Greisen, E. W., Yin, Q. F., Perley, R. A., Taylor, G. B., Broderick, J. J., 1998, AJ, 115, 1693

Croton, D. J., Springel, V., White, S. D. M., De Lucia, G., Frenk, C. S., Gao, L., Jenkins, A., Kauffmann, G., Navarro, J. F., Yoshida, N., 2006, MNRAS, 365, 11

Dunlop, J. S., Peacock, J. A., 1990, MNRAS, 247, 19

Fanaroff, B. L., Riley, J. M., 1974, MNRAS, 167, 31

Ferrarese, L., Merritt, D., 2000, ApJ, 539, 9

Francis, P. J., Hewett, P. C., Foltz, C. B., Chaffee, F. H., Weymann, R. J., Morris, S. L., 1999, ApJ, 373, 465

Furusawa et al. 2007, accepted by ApJS

Geach, J. E., Simpson, C. J., Rawlings, S., Read, A. M., Watson, M., 2007, astro − ph, arXiv : 0708.0982

Gebhardt, K., Bender, R., Bower, G., Dressler, A., Faber, S. M., Filippenko, A. V., Green, R., Grillmair, C., Ho, L. C., Kormendy, J. et al., 2000, ApJ, 539, 13

Goto, T., 2007, MNRAS, 381, 187

Granato, G. L., Danese, L., 1994, MNRAS, 268, 235

Hambly, N. C., Collins, R. S., Cross, N. J. G., Mann, R. G., Read, M. A., Sutorius, E. T. W., Bond, I. A., Bryant, J., Emerson, J. P., Lawrence, A. et al. 2007, arXiv:0711.3593

Heywood, I., Blundell, K. M., Rawlings, S., 2007, astro − ph, arXiv0708.1145

Hine, R. G., Longair, M. S., 1979, MNRAS, 188, 111

Ivison, R. J., Greve, T. R., Dunlop, J. S., Peacock, J. A., Egami, E., Smail, Ian, Ibar, E., van Kampen, E., Aretxaga, I., Babbedge, T., Biggs, A. D., Blain, A. W., Chapman, S. C., Clements, D. L., Coppin, K., Farrah, D., Halpern, M., Hughes, D. H., Jarvis, M. J., Jenness, T., Jones, J. R., Mortier, A. M. J., Oliver, S., Papovich, C., Prez-Gonzalez, P. G., Pope, A., Rawlings, S., Rieke, G. H., Rowan-Robinson, M., Savage, R. S., Scott, D., Seigar, M., Serjeant, S., Simpson, C., Stevens, J. A., Vaccari, M., Wagg, J., Willott, C. J., 2007, MNRAS, 380, 199

Jackson, C. A., Wall, J. V., 2001, ASPC, 227, 242

Jannuzi, B., Elston, R., Schmidt, G. D., Smith, P. S., Stockman, H. S., 1995, AJ, 454, 111

Johnston, H., Hunstead, R., Sadler, E., Cotter, G., Morganti, R., 2004, IAUS, 222, 451

Kennicutt, R. C., 1998, ARA&A, 36, 189

Lavalley, M., Isobel, T., Feigelson, E., 1992, ASPC, 25, 245

Lawrence, A., Warren, S. J., Almaini, O., Edge, A. C., Hambly, N. C., Jameson, R. F., Lucas, P., Casali, M., Adamson, A., Dye, S., et al., 2007, MNRAS, 379, 1599

Ledlow, M. J., Owen, F. N., 1996, IAUS, 175, 238

Liu, F. K., Wu, X-B., Cao, S. L., 2003, MNRAS, 340, 411

Lonsdale, C. J., Smith, H. E., Rowan-Robinson, M., Surace, J., Shupe, D., Xu, C., Oliver, S., Padgett, D., Fang, F., Conrow, T. et al., 2003, PASP, 115, 897

Magorrian, J., 2006, MNRAS, 373, 425

Martinez-Sansigre, A., Rawlings, S., Garn, T., Green, D. A., Alexander, P., Klckner, H. R., Riley, J. M., 2006, MNRAS, 373, 80

McLure, R. J., Dunlop J. S., 2004, MNRAS, 352, 1390

McLure, R. J., Willott, C. J., Jarvis, M. J., Rawlings, S., Hill, G. J., Mitchell, E., Dunlop, J. S., Wold, M. , 2004, MNRAS, 351, 347

Mortier, A. M. J., Serjeant, S., Dunlop, J. S., Scott, S. E., Ade, P., Alexander, D., Almaini, O., Aretxaga, I., Baugh, C., Benson, A. J., et al., 2005, MNRAS, 363, 563

Ogle, P., Whysong, D., Antonucci, R., 2006, ApJ, 647, 161

Owen, F. N., Laing, R. A., 1989, MNRAS, 238, 357

Pierre, M., Valtchanov, I., Alrieri, B., et al., 2004, J. Cosmol. Astro-Part. Phys., 9, 11

Rawlings, S., Saunders, R., 1991, Nature, 349, 138

Richards, G. T., Hall, P. B., Vanden Berk, D. E., Strauss, M. A., Schneider, D. P., Weinstein, M. A., Reichard, T. A., York, D. G., Knapp, G. R., Fan, X., Ivezic, Z., Brinkmann, J., Budavari, T., Csabai, I., Nichol, R. C., 2003, AJ, 126, 1131

Rowan-Robinson, M., 1995, MNRAS, 272, 737

Sarazin, C. L., Koekemoer, A. M., Baum, S. A., O'Dea, C. P., Owen, F. N., Wise, M. W., 1999, ApJ, 510, 90

Schoenmakers, A. P., de Bruyn, A.G., Rttgering, H.J.A., van der Laan, H., Mack, K.-H., Kaiser, C.R.. 1999, astro − ph/9910448

Sekiguchi, K., 2004, AAS, 205, 8105

di Serego Alighieri, S., Cimatti, A., Fosbury, R. A. E., 1993, ApJ, 404, 584

Serjeant, S., Rawlings, S., Lacy, M., McMahon, R, G., Lawrence, A., Rowan-Robinson, M., Mountain, M., 1998, MNRAS, 298, 321

Simpson, C., Martinez-Sansigre, A., Rawlings, S., Ivison, R., Akiyama, M., Sekiguchi, K., Takata, T., Ueda, Y., Watson, M., 2006, MNRAS, 372, 741

Tadhunter, C. N., Scarrott, S. M., Draper, P., Rolph, C., 1992, MNRAS, 256, 53

Tasse, C., Cohen, A. S., Rottgering, H. J. A., Kassim, N. E., Pierre, M., Perley, R., Best, P., Birkinshaw, M., Bremer, M., Liang, H., 2006, A&A, 456, 791

Vardoulaki, E., Rawlings, S., Simpson, C., 2006, astro − ph/0609719

Vardoulaki, E., Rawlings, S., Hill, G. J., Croft, S., Brand, B., Riley, J., Willott, C., 2006, AN, 327, 282

Willott, C. J., Rawlings, S., Blundell, K. M., Lacy, M., 2000, MNRAS, 316, 449

Willott, C. J., Rawlings, S., Jarvis, M. J., Blundell, K. M., 2003, MNRAS, 339, 173

APPENDIX A: NOTES ON THE 37 BRIGHTEST SXDS RADIO SOURCES

sxds_0001: The brightest radio source of our sample is a twin-jet (TJ) galaxy at redshift $z = 0.627$. Spectroscopy was obtained both with VIMOS on the VLT and ISIS on the WHT. In the latter case the slit width was 2.5 arcsec and the position angle PA $= 320°$. This object is resolved at K. The NVSS flux density is higher than the SXDS value (Table 1), indicating the existence of diffuse radio structure surrounding the radio source. This is a typical galaxy 'G', according to Sec. 3.3, with a prominent [OII] line in its optical spectrum and no hint of 24-μm emission. The apparent flattening between 610 MHz and 325 MHz maybe due to inaccurate flux density entry in the 325-MHz catalogue.

sxds_0002: This object has a classical double radio structure, as seen in the A-array radio map. It is also an obscured quasar 'OQ', since it has $\log_{10}(L_{24\mu m}/W) > 37.3$ and is resolved, and presumably dominated by starlight at K. Optical spectroscopy was obtained at the WHT using a slit with a width of 2.5 arcsec and a PA $= 305°$. The BRz-radio overlay in Fig.A1 shows the possibility of merging activity between the radio-source host galaxy and a nearby object.

sxds_0003: This is a classical double radio source since the A-array radio map reveals compact FRII-like hotspots associated with an obscured quasar at redshift 2.433. Spectroscopy was obtained both with VIMOS at the VLT and ISIS at the WHT, where in the latter case, the slit width was 2.5 arcsec and the PA $= 313°$. The optical spectrum lacks broad emission lines, a result that confirms our classification of this radio sources as 'OQ'. As in sxds_0002, the BRz-radio overlay reveals possible galaxy-galaxy merging activity and it has a 24-μm excess in its SED. The Lyα line in the emission spectrum of this object is spatially extended over ~ 3.4 arcsec $\simeq 25$ kpc.

sxds_0004: A compact flat-spectrum radio source with a SED rising to 24 μm. According to our classification scheme of Sec. 3.3, this is a BL Lac object, which is consistent with it having a flat radio spectral index ($\alpha = 0.164$). The difference between SXDS and NVSS flux densities (Table 1) indicates that the radio-source flux density might be time variable. This object was observed using AAOMEGA at the AAT, but we only have a 1-D spectrum available, with one highly questionable emission line at 5900 Å, and this does not give a reliable spectroscopic redshift; we prefer thus the photometric redshift.

sxds_0005: A compact steep-spectrum radio source and a galaxy without a secure spectroscopic redshift, since observations with the WHT didn't give a sufficient S/N to measure an accurate redshift (slit width 2.5 arcsec and PA $= 310°$). The optical spectrum shows a very faint continuum, as expected from its photometry (Simpson et al. 2006) and the fact that

the photometric redshift, $z = 1.610$, is in the 'redshift desert' where there is a lack of any strong emission lines.

sxds_0006: A compact radio source that is projected close to a bright star and hence without any entry in the mid-IR Spitzer catalogue. This object has no optical spectroscopy, but we are confident that the photometric redshift is accurate due to a good fit of the template to the SED (Fig. A1). It has an inverted spectral index, as calculated from the 1.4 GHz and 610 MHz data; the limit at 325 MHz verifies this result.

sxds_0007: A large (123 arcsec) FRII classical double radio galaxy at $z = 1.325$. The NVSS flux density is the sum of the integrated fluxes of the two lobes, which is the same value as the one measured from the NVSS map itself. Both 610 MHz and 325 MHz data suggest a very steep radio spectral index for this source.

sxds_0008: A compact radio source in a $z = 0.458$ blue galaxy. According to our classification of radio sources, this is a starburst 'SB' with a star formation rate SFR$_{FIR} \sim 100$ M$_\odot$yr^{-1}, calculated from the SED, using a Salpeter IMF and the star formation rate (SFR) relations of Kennicutt (1998). We have a good agreement of spectroscopic and photometric redshifts. From the BRz-radio overlay of Fig. A1 we see obvious galaxy-galaxy merging activity and a 24-μm excess in its SED. We believe the 24 μm excess is more readily attributable to a starburst than an AGN because the optical spectrum has bright [OII] emission but no corresponding high-excitation lines.

sxds_0009: A compact radio source missing $J-$ and $K-$band data since it lies outside the UDS coverage (Fig. 1). The weak extensions is the B-array radio map (Fig. A1) to the east and the south-west are probably artifacts. The high NVSS flux density is due to confusion with a nearby source. This object is probably at $z = 3.570$, which agrees with the photometric redshift (Table 1). The photometry of this object in the blue, B $= 26.3$ mag[††], indicates that the apparent blue tail in the optical spectrum is a spurious feature. This object has a flat radio spectrum and some evidence that a significant fraction of the optical light comes from a point source although there are no broad lines or a 24-μm excess. We classify it as a 'Q?' because of hints of broad wings to the Lyα line and the significant blue continuum, although the limit at 24-μm is insufficient to confirm a QSO-like mid-IR excess.

sxds_0010: A compact radio source and a galaxy 'G'. The HYPERz photometric code gives a good fit to the SED when we use the BC templates. There are no spectroscopic data available for this source.

sxds_0011: A radio galaxy at $z = 0.647$ with TJ structure. The angular size was measured from the ra-

[††] ($www.astro.livjm.ac.uk/ \sim cjs/SXDS/radio/$)

dio overlay from the core to the largest extent of the north-east jet and separately to the south-east radio components, with the two values added together. The 610 MHz flux density was measured around the same area as the 1.4 GHz flux density giving a radio spectral index between these values of 0.62. The NVSS flux density, though, suggests that there is extra emission at large angular sizes. We adopt a typical steep radio spectral index of $\alpha = 0.8$ since steep spectral indices are typical for objects with a FRI radio structure; the spectral index calculated from the SXDS and 325 MHz data suggests an inverted spectral index which is inconsistent with the fact that this is a large twin-jet radio source. We suggest that the 325 MHz data are inaccurate in this case.

sxds_0012: A large FRII galaxy at $z = 0.865$. The 325-MHz catalogue entry includes only part of the source, giving a nonsensical radio spectral index. We use the total 610-MHz flux density from the radio map to calculate the spectral index, whose steep value agrees with the CD radio structure. There are no signs of a QSO nucleus.

sxds_0013: A spectroscopically confirmed quasar at $z = 2.713$ and a point source in the optical. The optical spectrum shows strong absorption features associated with the broad lines. Such broad-absorption-line (BAL) QSOs are rare, but not unknown, in radio-selected samples. The B-array radio image shows a compact source. From the optical overlay of Fig. A1 it looks like a galaxy is dominant in the $K-$band, since it is not a point source at K, although it is one in the optical. The flat radio spectral index, $\alpha = 0.08$, agrees with the fact that this is a compact radio source.

sxds_0014: This object appears to be red with a rapid drop in its SED from red to blue. In the $K-$band image, although it has a low S/N ratio, the source looks unresolved indicating that the radio source might be compact or there is a hidden quasar nucleus. The limit at 24 μm is insufficient to rule out that this might be an obscured quasar 'OQ'; we define it as a galaxy 'G?' (see Sec 3.3). In Vardoulaki, Rawlings & Simpson (2006) we used 36 radio sources from this sample, accidentally excluding this one; all the subsequent identification numbers have moved downwards in order to include this radio galaxy. The inverted radio spectral index is consistent with the fact that this is object has compact radio structure. The tentative emission feature around $\lambda \sim 6000$Å in the optical spectrum of this object cannot provide us with a reliable spectroscopic redshift.

sxds_0015: A possible 'double-double' radio galaxy. Such sources (Schoenmakers et al. 1999) are thought to be jets that have re-started, sometimes (as perhaps in this case) with a change of jet orientation, perhaps due to merging of two supermassive binary black holes (Liu et al. 2003). From the BRz-radio overlay of Fig. A1 we see evidence of galaxy-galaxy merging in the form of tidal tails (Johnston et al. 2004), and there is also excess emission at 24 μm

as can be seen in its SED. We use the radio spectral index calculated between 610 MHz and 1.4 GHz data, which gives a steep value that agrees with the FD radio structure. We don't trust the 325 MHz data since they give a spectral index inconsistent with the radio structure. Although this object is defined as 'G', its detection at 24 μm might indicate it is either a 'SB' or a 'WQ'.

sxds_0016: A classical-double radio source, possibly at $z = 1.345$. Shorter wavelengths in the spectrum are, due to poor resolution, affected by the overlapping spectrum of a nearby object. Photometry of this object was directly measured from images using sxds_0034 as a boot-strap calibrator, since it was not matched with any source within a $2''$ search radius. Using these data we give the photometric redshift in Table 1 with an associated uncertainty. According to these measurements, the object has excess emission at 24 μm, which classifies it a 'OQ' according to Section 3.3 and Fig. 3. We use the spectral index calculated between the 610 MHz and 1.4 GHz flux densities, which agrees with the CD radio structure of this object.

sxds_0017: A spectroscopically-confirmed broad-absorption-line quasar at $z = 2.583$, where the Lyα line is heavily absorbed. The spectrum appears peculiar, since the CIV and CIII] lines have narrow cores and a red and blue broad wing respectively. The radio map reveals a prominent hotspot to the northeast; the component to the south-west of the quasar is probably the weak side of an asymmetric double. We use the 325 MHz flux density to calculate a spectral index since it was not observed at 610 MHz.

sxds_0018: A large FD (no compact hotspots in the A-array map) radio galaxy at $z = 0.919$. The radio spectral index is calculated between the 610 MHz and 1.4 GHz data, where the steep value is consistent with the extended FD radio structure. The 325-MHz catalogue entry is probably inaccurate, since plausible extrapolation of the 610 MHz flux density suggests that the object has more flux density at 325 MHz than the limit of that catalogue.

sxds_0019: A FD (no compact hotspots in the A-array map) radio galaxy at $z = 0.694$. It has a very asymmetric radio structure. We assume $\alpha = 0.8$ due to the extended FD radio structure; the inverted spectral index calculated between the 325-MHz and 1.4-GHz data is inconsistent with the radio structure of this object.

sxds_0020: This object has an unusual radio structure that we classify, uncertainly, as FD. The steep spectral index calculated between 610 MHz and 1.4 GHz is consistent with the extended radio structure. The 325-MHz entry is inaccurate since both the radio structure and the 610-MHz to 1.4-GHz spectral index indicate that it has a steep radio source. There are no spectroscopic data available for this object and the photometric estimate is highly uncertain.

sxds_0021: A radio galaxy 'G' and a compact radio source. The radio structure to the north-west side of the object is probably not associated with the brightest radio source as it has a separate galaxy identification. The photometric redshift is used since there is no spectroscopy available.

sxds_0022: A compact radio source associated with a galaxy at $z = 0.248$; note the spectacular blue arc which is probably a remnant of star formation associated with a galaxy-galaxy interaction. The southern and eastern radio components are probably artifacts. This is possibly a post-starburst galaxy, or an 'E+A', i.e. an elliptical with additional absorption lines (e.g. Hβ in Fig.A1) in their optical spectra due to stars seen $\sim 10^8$ yr after the starburst has finished (Goto 2007). Star formation might be contributing to the radio emission. There is some evidence for excess emission at 24 μm as well as dramatic tidal tails (Fig. 1). We classify this radio source as a 'G'.

sxds_0023: A compact radio galaxy at $z = 0.586$. The A-array map reveals a possible double structure, although it might be the base of a FRI-like jet. There is a fairly good agreement between the spectroscopic and photometric redshifts.

sxds_0024: A TJ radio galaxy at $z = 0.516$. The radio spectral index that is calculated between 325 MHz and 1.4 GHz is inconsistent with the TJ radio structure of the source; so we use 610 MHz flux density.

sxds_0025: A compact weak quasar 'WQ' probably at $z = 0.9636$ if the single marginally broad line in the spectrum is MgII (the deconvolved FWHM is $\sim$ 900 kms^{-1}). We are not certain that the [OII]λ2470Å emission line is real, since spectroscopic studies show that this is quite a weak feature (e.g. Serjeant et al. 1998). The photometric redshift is inaccurate due to the absence of $J-$ and $K-$band data (Fig. 1) and the fact that the optical continuum appears to be dominated by blue QSO light; the rest-frame EW of the putative MgII line is $\sim$ 50 Å and thus within the spread seen in directly viewed quasar nuclei (Francis et al. 1999). The templates used in the HYPERz code cannot provide a proper fit to the SED. The NVSS flux density is higher than expected due to confusion by sxds_0027. This object was not observed at 610 MHz since it is outside the coverage of the survey. We assign a typical flat radio spectral index $\alpha = 0.4$ consistent with the compact radio structure; we do not trust the 325-MHz catalogue to be complete.

sxds_0026: A TJ radio galaxy at $z = 0.450$. The companion galaxy to the west is probably not producing radio emission. According to the radio spectral index calculated between 610 MHz and 1.4 GHz data, this is a steep-spectrum radio source. The fact that the 325-MHz entry is a limit suggest that we should not trust that the 325-MHz catalogue is complete.

sxds_0027: We classify this object as 'OQ' since it has excess emission at 24 μm. We use the photometric redshift since the optical spectrum shows a fea-

tureless continuum. The longer-wavelength SED looks more like a BL Lac since it can easily be fitted by a power-law with very steep spectral index $\alpha \sim 2$, and is consistent with the flat continuum in the optical spectrum of this object. The 'tails' in the radio map are probably artifacts, so its compact nature is consistent either with it being a BL Lac object or an 'OQ'. The object is resolved at K which is why we prefer the 'OQ' category. This radio source is not observed at 610 MHz. We assign a typical flat radio spectral index $\alpha = 0.4$ consistent with the compact radio structure; we do not trust the 325-MHz catalogue to be complete at the flux density level appropriate to this source. The NVSS flux density is higher than expected since with the NVSS resolution we can only marginally distinguish this object from the nearby object sxds_0025.

sxds_0028: A compact radio galaxy, probably at $z = 0.627$. The radio map shows a seemingly double source, but in reality there are two radio sources, as there are good optical IDs under both apparent radio lobes. The object under the north-west 'lobe' is sxds_0028, whereas the one under the south-east 'lobe' is sxds_0042 (a compact radio source at redshift $z = 0.382$, which is just below our flux density limit). The flattening of the radio spectral index between 610 MHz and 325 MHz suggests that the 325-MHz catalogue is incomplete; the 325 MHz flux should be higher than the limit of that catalogue.

sxds_0029 A compact radio source that looks unresolved in the $K-$band. Due to absence of spectroscopic data, we use the photometric redshift, which suggests a fairly good fit to the SED (Fig. A1).

sxds_0030: This probably is a TJ radio galaxy at redshift $z = 0.535$ with the jets swept back forming a narrow-angle tail. There is a fairly good agreement between the photometric and spectroscopic redshifts.

sxds_0031: This is a compact radio galaxy. The radio component to the west is probably not associated with this source as it has its own separate galaxy identification. The fairly good fit of the photometric redshift makes us confident to use it in the absence of spectroscopic data.

sxds_0032: This is probably a FD radio galaxy; no A-array data available to confirm lack of compact hotspots. Without any spectroscopic redshift, the BC templates provide a very good fit to the photometric data and a believable photometric redshift. The 325-MHz catalogue misses this object. According to the spectral index calculated between the 610 MHz and 1.4 GHz data, this object should have a flux density at 325 MHz that would give a steep spectral index.

sxds_0033: A TJ radio source at $z = 0.647$. It belongs to a small group of galaxies that is interacting and probably merging with a larger group of galaxies (Geach et al. 2007). The feature at 5426 Å in the optical spectrum (Fig. A1) is CIII] emission from a lensed background object at $z = 1.847$ (see Geach et al. 2007). It is not clear whether the excess emission

at 24 μm is associated with the lens or the galaxy. However, the majority of the radio emission probably originates in the lensing source. The steep spectral index calculated between 610 MHz and 1.4 GHz data indicates that the 325 MHz flux density should be higher than the catalogue entry.

sxds_0034: A compact radio source at $z = 1.095$ with a clear QSO component at the wavelengths probed by Spitzer data, a point-like optical structure, and high-excitation narrow lines in its spectrum. It is, most plausibly, a Doppler-boosted object with low extinction and possible time variability. This is the one object with significant accretion that lies below the FRI/FRII break (Fig. 6), indicating that it is a FRI 'radio-quiet' quasar.

sxds_0035: A compact radio source and a galaxy without spectroscopy or $J-/K-$band data. The HYPERz code fits the 4000 Å break between J and K, which gives a photometric redshift of $z = 2.715$.

sxds_0036: A compact radio source and a galaxy 'G' at $z = 0.871$. The 610 MHz flux density is an upper limit, giving an uncertain measurement for the radio spectral index.

sxds_0037: A compact radio source and a galaxy 'G' that is not observed in the J and K band (Fig. 1), and which therefore has a tentative photometric redshift. This radio source was outside the coverage of the 610 MHz survey. We use a typical flat radio spectral index $\alpha = 0.4$, consistent with the compact radio structure of this source; we don't trust the 325-MHz catalogue to be complete at this flux density level.

Figure A1. *Top:* K-band images and overlaid radio contours from the VLA for sxds_0001; either the B/C-array (beam $\simeq 4$ arcsec^2) or the A/B/C-array map (beam $\simeq 1.8$ arcsec^2) is shown, with the image labelled as B or A respectively. For sxds_0009, sxds_0017, sxds_0025, sxds_0027 and sxds_0037 there are no K-band images since these objects are beyond the edge of the UDS survey (see Fig. 1), so we use z-band images instead. The radio structural classification is shown on the bottom right of the image. *Second from top:* Overlays of $B-$, $R-$ and $z-$band images and B-array radio maps from Simpson et al. (2006). *Second from bottom:* Observed frame SEDs of our objects, where we also give the best-fit SEDs, their spectroscopic redshift $z_{\rm spec}$ (where applicable) and their photometric redshift calculated from HYPERz: the red SED is calculated using BC templates and the black with CWW templates (see Section 3.2). In all the overlays, North is up and East is to the left. The contour levels follow: $2^{n_{\rm contour}-1} \times \sigma$, where $n_{\rm contours}$ is the number of contours and σ the noise level. *Bottom:* Optical spectra of 25 of the 37 SXDS radio sources. The character 'A' denotes atmospheric absorption feature, 'S' a featured caused by the dichroic, 'C' a cosmic ray, and 'F' fringing on the CCD. All spectra have been smoothed over 3 pixels. The following spectra are not flux calibrated: sxds_0009, sxds_0028, sxds_0030.
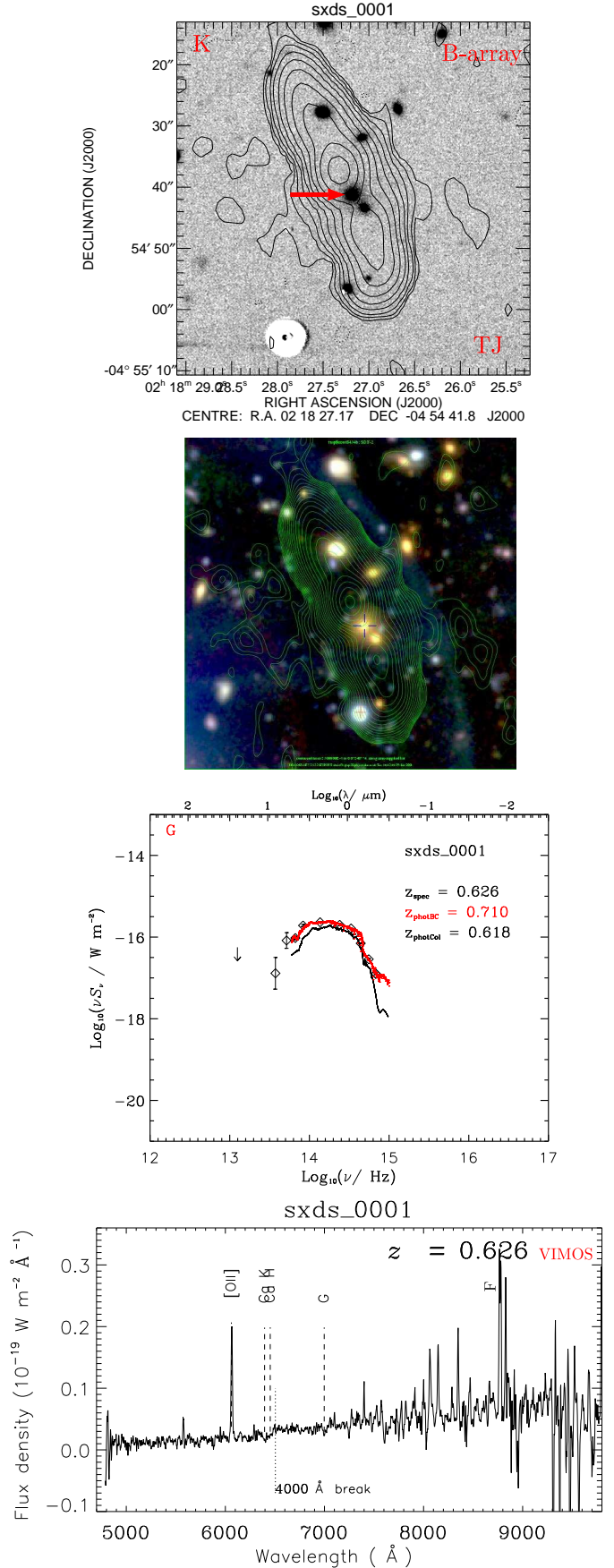
Figure A1. The rest of Fig. A1 can be found at the URL: $www - astro.physics.ox.ac.uk/ \sim eleniv/figure\_A1.html$